

The association between gas and galaxies III: The Cross-correlation of Galaxies[†] and Ly- α Absorbers[‡] at $z \sim 1$

Allen M. Shone^{*1} Simon L. Morris¹ Neil Crighton¹ Richard J. Wilman²

¹*Department of Physics, University of Durham, South Road, Durham, DH1 3AJ, UK.*

²*Centre for Astrophysics & Supercomputing, Swinburne University of Technology, Hawthorn, Victoria 3122, Australia.*

Accepted 0000 January 00. Received 0000 January 00; in original form 0000 January 00

ABSTRACT

We have measured the 2D 2-point correlation function, ξ_{AG} , between low column density Ly- α absorbers and galaxies at a redshift $z \sim 1$. We measured Ly- α absorbers between redshifts $z = 0.68 \rightarrow 1.51$ over a total redshift path length of $\Delta z = 1.08$ from HST STIS E230M absorption spectra towards the quasars HE 1122-1648 ($z = 2.4$) and PKS 1127-145 ($z = 1.187$). The column density of the Ly- α absorbers ranged from $13.2 \leq \log_{10}(N_{HI}(\text{cm}^{-2})) \leq 17.4$, with a median column density of $\log_{10}(N_{HI}(\text{cm}^{-2})) = 14.0$. A total of 193 galaxy redshifts within the surrounding $6.8' \times 5.7'$ field of view of both quasars were identified in a R magnitude limited survey ($21.5 \leq R_{Vega} \leq 24.5$) using the FORS2 spectrograph at the VLT, of which 95 were higher than the minimum redshift of $z = 0.68$ to be used in the correlation function. A 3σ upper-limit of $\xi_{AG} = 2.8$ was found when 145 Ly- α absorber-galaxy pairs were binned in redshift space, in a bin of size $\Delta\sigma = 1.0$, $\Delta\pi = 2.0 h_{70}^{-1}$ Mpc along the projected separation and line of sight distances respectively.

The upper-limit in the cross-correlation was found to be 5.4σ lower than the central peak in the galaxy auto-correlation within the same redshift range, ξ_{GG} , which was in our data equal to 10.7 ± 1.4 . Thus we have shown for the first time that the clustering between low column density absorbers and galaxies at a redshift of 1 is weaker than that between galaxies at the same redshift.

Key words: galaxies – intergalactic medium, galaxies – quasars: absorption lines, galaxies – galaxies: haloes.

1 INTRODUCTION

This paper is the third in a series that investigates the extent to which Ly- α absorbers in the inter-galactic medium (IGM) are associated with galaxies.

At the current epoch only a minor fraction of the

baryons in the universe exist within galaxies. Stars, galaxies and other stellar remnants make up 6% of the baryonic matter density of the universe, Ω_b , while within the galaxies cold ($T \lesssim 10^4$ K), condensed gas contributes a further $\sim 1.7\%$ (Bregman 2007). Therefore at least 90% of baryons in the universe lie beyond the galaxies, in the IGM.

Part of this remaining fraction, which is only 10 – 100 times the mean cosmic density, is more susceptible to shock heating. Shock waves that are caused by gravitational collapse travel along the filamentary structure heating the gas to $T = 10^5 - 10^7$ K. These baryons form the diffuse warm-hot intergalactic medium (WHIM) (Cen & Ostriker 1999; Fukugita et al. 1998). The detection and study of the WHIM using metals detected in ultra-violet (Verner et al. 1994; Tripp & Savage 2000; Danforth & Shull 2005; Thom & Chen 2008) and x-ray spectroscopy (Nicastro et al. 2002; Fang et al. 2006) is a major science motivation for the future space instruments XEUS (the X-Ray Evolving Universe Spectrometer) and the

[†]Based on observations collected at the European Organisation for Astronomical Research in the Southern Hemisphere, Chile. ESO programme number 076.A-0312.

[‡]Based on observations made with the NASA/ESA Hubble Space Telescope, and obtained from the Hubble Legacy Archive, which is a collaboration between the Space Telescope Science Institute (STScI/NASA), the Space Telescope European Coordinating Facility (ST-ECF/ESA) and the Canadian Astronomy Data Centre (CADAC/NRC/CSA). Additional data based on observations from the UVES spectrograph was collected at the European Organisation for Astronomical Research in the Southern Hemisphere, Chile. ESO programme numbers 067.A-0567(A), 068.A-0570(A) and 069.A-0371(A).

*E-mail: a.m.shone@durham.ac.uk

new COS (Cosmic Origins Spectrograph) on the Hubble-Space Telescope (HST).

A third of the gas that remains is probably located in the diffuse IGM at temperatures $T \sim 10^4 - 10^5$ K (Sembach et al. 2004; Lehner et al. 2007; Danforth & Shull 2008). The neutral fraction of this ionised plasma is observed in quasar absorption spectra. Under the influence of dark matter this gas is thought to have collapsed to form clouds that are part of a filamentary network that traces the layout of the galaxies. Two original opposing models questioned whether this gas is correlated with galaxies but is part of the giant cosmic web (Morris et al. 1993), or whether the clouds are discrete and isolated with the gas contained within galaxy haloes (Lanzetta et al. 1995).

Even though opinion is siding with the former there is probably no definitive answer to this question, as the typical location of these clouds is expected to be a function of their column density. At $\log_{10}(N_{\text{HI}}(\text{cm}^{-2})) \sim 21$, the density of gas in an absorber would be comparable to that in the outer regions of a galaxy. Therefore at a small separation it would be pointless to draw a line where a galaxy terminates and the absorber begins. In the low (Rao et al. 2003; Zwaan et al. 2005) and intermediate redshift universe (Le Brun et al. 1997; Chen & Lanzetta 2003) clouds with a column density $\log_{10}(N_{\text{HI}}(\text{cm}^{-2})) \gtrsim 20.3$, (the damped Ly- α absorbers systems) have been shown in imaging and spectroscopy to be associated with galaxies. Meanwhile those clouds with a column density several decades less dense, $\log_{10}(N_{\text{HI}}(\text{cm}^{-2})) \leq 14$, are more likely to make up the filaments or lie in the voids of the IGM. The absorber-galaxy association is also dependent on the epoch, for example because of the decrease in the number density of Ly- α lines since redshift $z \sim 1.7$ (Sargent et al. 1980; Bahcall et al. 1991; Janknecht et al. 2006).

1.1 The Issues to Resolve and Investigations so far

The 2D 2-point cross correlation between Ly- α absorber and galaxy positions is a powerful way to quantitatively measure the relationship between galaxies and the IGM. It is hoped that these measurements will provide an insight into the degree of association between galaxies and the surrounding neutral gas. The degree of correlation is thought to depend on the redshift, the column density of the absorbing cloud, the galaxy magnitude, the presence of a galactic wind, and the line-of-sight distance and projected separation (distances π and σ) between the galaxy and the absorber.

A common way to analyse the Ly- α absorber-galaxy cross-correlation is to contrast the results with the galaxy auto-correlation. If these values are comparable or the cross-correlation is greater at small separation, then the Ly- α absorbers could be claimed to be more of a feature of the galactic halo rather than the IGM.

We now give a short overview of such measurements that have been made over different redshifts.

1.1.1 Observations at Low Redshift

Ryan-Weber (2006) (hereafter RW06) studied the HI-galaxy correlation at redshifts $z \sim 0$. 5317 gas rich galaxies that

were detected in the HIPASS galaxy survey (Zwaan et al. 2003) were correlated with 129 absorbers from 27 lines of sight. These spectra were gathered from STIS and GHRS data and all absorbers had $\log_{10}(N_{\text{HI}}(\text{cm}^{-2})) = 12.41 - 14.81$.

It was found that at small separations there is a strong correlation between absorbers and gas rich galaxies that is similar in strength to the galaxy auto-correlation function. This supports the idea of matter clustered within the vicinity of galaxies (within the nodes of the cosmic web) be they absorbing clouds or other galaxies. However, unlike the galaxy auto-correlation that decays radially along the σ and π direction, ξ_{AG} remained high out to $10 \text{ h}^{-1} \text{ Mpc}$ or 1000 km s^{-1} along the line of sight. The proposed origin of this was the accretion of gas. In this scenario the gas falls in from the more diffuse IGM, drains along filaments and falls into a galactic halo causing an elongation in the redshift space correlation along the line of sight. The gas rich galaxies that were detected using 21 cm radiation also tended to have a low mass ($M \sim 10^8 M_{\odot}$), and it is galaxies such as these that Kereš et al. (2005) claims are dominated by this method of accretion.

1.1.2 A simulation of ξ_{AG} at low redshift

The results of RW06 were compared with simulations in Pierleoni et al. (2008). Three simulations, each with a different galaxy wind model were run to a redshift of zero. Either no winds, strong winds or extremely strong winds were present.

Spectra were generated from 999 sightlines that sampled the simulation. The Ly- α absorbers that had a column density in the range $\log_{10}(N_{\text{HI}}(\text{cm}^{-2})) = 12.41 - 14.81$ were then correlated with ~ 5000 galaxies that resided in haloes of mass $M = 8 \times 10^{10} - 10^{13.5} M_{\odot}$. However, contrary to RW06, Pierleoni et al. (2008) found the galaxy auto-correlation was predicted to be stronger than the absorber-galaxy cross-correlation.

The correlation function was recalculated using only 27 sightlines to match the sample from RW06, and the sample noise increased. Bootstrap errors showed a difference between ξ_{AG} and ξ_{GG} at only a 1σ significance level. Pierleoni et al. (2008) suggest that it is this sparse sampling that make the cross and auto-correlation functions indistinguishable. They also attribute the large ‘‘finger-of-god’’ observed in Figure 3 of RW06 to this effect.

1.1.3 Observations at low to intermediate redshift

(i) *Chen & Mulchaey (2009); Chen et al. (2005)*

Chen et al. (2005) studied the sightline towards PKS 0405-123, and compared the positions of 112 Ly- α absorbers from STIS echelle spectra with 482 galaxies within the redshift range $z = 0.1 \rightarrow 0.5$. These were collected using a magnitude limited survey down to $R \leq 20$.

The most striking result found by Chen et al. (2005) was a difference in the level of correlation that depended on whether the galaxy in question was dominated by emission or absorption spectral lines. The correlation function between galaxies that were dominated by emission, and Ly- α absorbers that had $\log_{10}(N_{\text{HI}}(\text{cm}^{-2})) \geq 14.0$, was found

to be similar to the galaxy auto-correlation. No significant cross-correlation was seen for those galaxies dominated by absorption.

Chen & Mulchaey (2009) then expanded on this result with two further lines of sight towards quasars HE 0226-4110 and PG 1216+069. It was found that within a projected separation of $1 \text{ h}_{100}^{-1} \text{ Mpc}$ Ly- α absorbers with $\log_{10} (N_{\text{HI}} (\text{cm}^{-2})) \geq 14$ had a similar cross-correlation with galaxies as the auto-correlation of emission line dominated galaxies. This was ~ 6 times weaker than the self-clustering of absorption line dominated galaxies. They suggest that the cross-correlation was similar between emission dominated galaxies and Ly- α absorbers because both these occupy the same halo system.

The cross-correlation between any type of galaxy and Ly- α absorber with $\log_{10} (N_{\text{HI}} (\text{cm}^{-2})) \leq 13.5$ was observed to be very weak.

(ii) *Papers I and II*

This paper is an extension to the investigation first conducted in paper I, Morris & Jannuzi (2006) (hereafter MJ06). Here the location of 636 galaxies, with redshifts determined using CFHT spectroscopy, were compared with 381 Ly- α absorbers found in the UV spectra of quasars taken with the Faint Object Spectrograph during the Hubble Key Project. It was found that, excluding the high column density systems ($\log_{10} (N_{\text{HI}} (\text{cm}^{-2})) \geq 17$), absorbers are correlated with galaxies at redshifts of $z \leq 0.8$ and that this correlation is weaker than the corresponding galaxy auto-correlation.

Paper II (Wilman et al. 2007) (hereafter W07) using the MJ06 dataset computed the 2-point correlation function along the line-of-sight (π) and projected separation (σ). A conclusion drawn from this work suggested that at small co-moving separations of $\sigma < 0.4$, $\pi < 2 \text{ h}^{-1} \text{ Mpc}$, the correlation function increases marginally as the column density increases from $\log_{10} (N_{\text{HI}} (\text{cm}^{-2})) = 13 - 16$, then there is suggestion of a sharp increase in correlation above $\log_{10} (N_{\text{HI}} (\text{cm}^{-2})) \geq 17$. This was proposed as tentative evidence for the column density at which absorbers become a part of the galactic halo.

It was argued in W07 that a “finger-of-god” may also be caused by a large anisotropy, for example a quasar line of sight that runs parallel and close to a large filament. However Pierleoni et al. (2008) ruled out a “finger-of-god” being caused by this geometric effect in their simulation by showing that the ξ_{AG} result remained the same no matter which orientation the sightlines had been directed. Instead a “finger-of-god” was caused if a sightline passed through a virialised system of gas and a paired galaxy.

1.1.4 *Observations at high redshift*

In order to observe the IGM-galaxy relationship at high redshift (where the Ly- α absorption has now reached optical wavelengths) Adelberger et al. (2003) correlated the Ly- α lines from 8 quasar HIRES or ESI spectra with 431 Lyman-break-galaxies.

It was expected that greater concentrations of gas would be located near to the galaxies. This was found to be so as gas with a greater optical depth than the mean density was

found to lie within $\sim 10 \text{ h}^{-1} \text{ Mpc}$ of the nearest galaxy. However, evidence arose of an anti-correlation within $\sim 0.5 \text{ h}^{-1} \text{ Mpc}$. It was hypothesised that this was caused by superwinds that, travelling at $\sim 600 \text{ km s}^{-1}$ (Pettini et al. 2001), clear the immediate vicinity of the galaxies and heat the surroundings, decreasing the neutral fraction of HI and so increasing the transmission of QSO flux.

With a larger data set of 23 sightlines and 1044 UV selected galaxies Adelberger et al. (2005) found that evidence for an anti-correlation at small separation significantly decreased. Only in a third of the cases was weaker absorption now detected around galaxies.

1.2 **The motivation for this work**

No results have been obtained for the redshift window $z \sim 1$. The main reason for this is the difficulty of acquiring a sufficient number of galaxy redshifts at this epoch that are within the same fields of view as quasars for which there is high resolution UV echelle spectral data. The aim of this investigation was to start to bridge this gap.

Thus we hope to shed light on the Ly- α absorber-galaxy correlation at redshifts $z \sim 1$. Then by comparison with the other works mentioned above determine whether the correlation evolves with redshift.

The structure of this paper will be as follows. The data reduction for the FORS2 galaxy survey and absorbers from the HST STIS E230M spectra will be described in Sections 2 and 3 respectively. In Section 4 the basics of the 2D 2-point cross correlation function used will be outlined. Results are given in Section 5 and we present our discussion and conclusions in Section 6.

Throughout the paper we have adopted the cosmological parameters $\Omega_{\text{M}} = 0.3$, $\Omega_{\Lambda} = 0.7$, $h_{70} = 0.7$ and $H_0 = 100h_{70} \text{ km s}^{-1} \text{ Mpc}^{-1}$.

2 **THE GALAXY SURVEY**

Galaxy surveys in two $6.8' \times 5.7'$ regions around the quasars HE 1122-1648 ($z = 2.40$) and PKS 1127-145 ($z = 1.187$) (Carswell et al. 2002; Bechtold et al. 2002) were carried out using the FORS2 spectrograph at the VLT on the 20-22 February 2006 (Appenzeller et al. 1998). The total wavelength range of the absorbers to be used in the archived HST STIS data was between 2050-3100 Å. This means we could potentially detect Ly α absorbers between the redshifts of 0.68 and 1.55. It was our aim to observe galaxies within a similar redshift window. This was done by selecting galaxies based on a magnitude limit ($21.5 \leq m_{\text{R}} \leq 24.5$) and using FORS2 to detect [O II] emission appearing in the 5600-11000 Å bandpass. It is thought these [O II] emitters, indicative of star-forming galaxies, with their systems of feedback, outflows and photoionisation are responsible for most of the complexity in the gas-galaxy relationship at $z \sim 1$.

2.1 **Pre-imaging and mask generation**

Prior to the Multi-Object-Spectroscopy (MOS) observing run pre-imaging was taken in service mode of the two quasar fields using the Bessel R_SPECIAL+76 filter. Photometric conditions with good “seeing” (≤ 0.8) was requested for each

Table 1. The quasar field coordinates

Quasar	RA range (J2000)	DEC range (J2000)
PKS 1127-145	11 30 21.57 : 11 29 52.50	-14 53 34.84 : -14 45 54.81
HE 1122-1648	11 24 57.47 : 11 24 28.07	-17 09 25.71 : -17 01 45.68

10 minute exposure in order to attain accurate astrometry and photometry when selecting faint ($R \leq 24.5$) galaxies.

Table 1 shows the areas of sky that were included.

These images were reduced using the FORS2 imaging pipeline at ESO headquarters in Garching as part of the routine service mode. Calibration data had also been taken at the same time, including bias frames, sky flats and photometric standard images. Using this calibration data the raw images were bias subtracted, flat-fielded and cosmic rays were removed.

We performed the final stages needed to reduce the science images locally using the standard IMUTIL tasks within IRAF.¹ The overscan region of each frame was cropped and then images taken from chips 1 and 2 were joined together using IMTILE.

The software Source Extractor (v2.4) (Bertin & Arnouts 1996) was then run in order to compile a catalogue of all the possible targets for follow-up spectroscopy.

SExtractor was used to calculate the photometry of every target and classify each target according to whether it is a star or galaxy. The relevant parameters were MAG AUTO, an estimate of the apparent magnitude enclosed within an ellipse that encompasses 90% of the the flux, and CLASS STAR.

The magnitude zero point was determined by measuring the total counts of exposed standard stars within the image foreground and comparing these flux values with that of their magnitude in the USNO-A2.0 star catalogue.

Figure 1 shows a plot of CLASS STAR against apparent magnitude (m_R) for all the 2666 objects extracted from the field of HE 1122-1648. One can tell that the reliability of CLASS STAR decreased as the targets become fainter. A cut of CLASS STAR ≤ 0.8 was made to select galaxy candidates (Cristóbal-Hornillos et al. 2003).

This plot also gave an indication as to what would be an effective faint magnitude cut-off. To avoid those targets where CLASS STAR was ambiguous a faint cut of $m_R \leq 24.5$ was chosen. The minimum brightness was also set by what could be successfully observed within the allotted exposure time. To remove those foreground galaxies likely to have redshifts too low to correlate with the HI absorbers, a bright cut-off of $m_R \geq 21.5$ was employed.

2.1.1 Making the masks

The final catalogues consisted of 1062 and 1122 objects in the fields of HE 1122-1648 and PKS 1127-145 respectively.

¹ IRAF is distributed by the National Optical Astronomy Observatory, which is operated by the Association of Universities for Research in Astronomy (AURA) under cooperative agreement with the National Science Foundation.

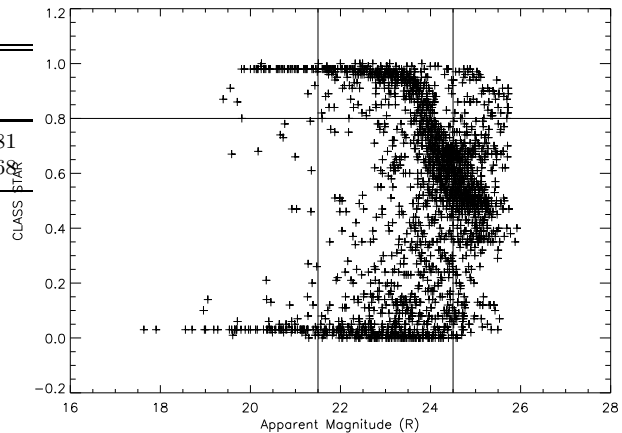


Figure 1. This horseshoe-shaped plot of the CLASS STAR classification against magnitude allowed cuts to be made so that galaxies within the enclosed rectangle could be included in the galaxy catalogue to be sent to the mask making software. Those selected had $21.5 \leq m_R \leq 24.5$ and $0 \leq \text{CLASSSTAR} \leq 0.8$.

The lists were then passed to the FIMS software for the FORS2 instrument that designs custom masks for the mask-exchange-unit (MXU).

We designed rectangular slits $1''$ by $8''$. This meant that all targets took up no more than $1/4$ of the length of the slit, allowing ample space for sampling the sky so that it could be subtracted later. The slit sizes and the galaxy density meant that up to 50 slits could be made per mask.

When investigating 2D 2-point correlation functions it is important that the slits are assigned randomly so as not to bias a particular absorber-galaxy/galaxy-galaxy angular separation. Therefore a random slit allocation was used in FIMS to ensure a random distribution of galaxies was selected when designing each mask.

It was also important to obtain more than one mask per field-of-view to allow sampling of close pairs.

The catalogue was split between those galaxies with $21.5 \leq m_R \leq 23.5$ and $23.5 \leq m_R \leq 24.5$ so that separate “bright” and “faint” masks would be used. They could then be exposed for different periods of time. This allowed us to optimise the exposure times used to reach a given signal-to-noise ratio for each mask - shorter exposure times for bright masks, and longer times for faint masks. Altogether 22 masks were designed with each mask containing approximately 40 slits. There were 11 for each field-of-view, including 5 that were assigned bright objects and 6 that had slits over galaxies with $23.5 \leq m_R \leq 24.5$.

2.2 Details of the observing run

The FORS2 MXU was used in visitor mode with the R_SPECIAL+76 filter and the 200I+28 grism. This grism gave a central wavelength of 7450 \AA with a spectral range of $5600 \rightarrow 11000 \text{ \AA}$. The dispersion was $2.43 \text{ \AA pixel}^{-1}$ with a resolution $\frac{\lambda}{\Delta\lambda} = 380$ (Jehin & O’Brien 2007).

The plan for the first night of observation (MJD 53787) was to concentrate on PKS 1127-145 with 5 “faint” masks and 5 “bright”. Very poor ‘seeing’ conditions ($\sim 1.4''$) and high winds hampered the first night of observing and it was

Table 2. The galactic spectroscopy that was carried out

Mask name	No. of Exposures and time (s)	Mean 'Seeing'	Comments
1127 "Bright" 1	3 x 650	1.7''	...
1127 "Faint" 1	2 x 1650	1.4''	No continuum
1127 "Faint" 2	2 x 1650	1.0''	Few sources
1127 "Bright" 2	3 x 650	1.0''	...
1127 "Bright" 3	3 x 650	0.80''	...
1127 "Bright" 4	3 x 650	0.80''	...
1127 "Bright" 5	1 x 650	1.7''	...
1122 "Bright" 1	2 x 1750	1.0''	TOO
1122 "Bright" 2	2 x 1750	0.75''	...
1127 "Bright" 1	2 x 1750	0.65''	...
1127 "Bright" 2	1 x 1750	0.50''	...
1127 "Bright" 3	1 x 1750	0.65''	...
1127 "Bright" 4	1 x 1750	0.65''	...
1127 "Bright" 5	2 x 1350	0.65''	...
1122 "Bright" 3	2 x 1350	0.65''	...
1122 "Bright" 4	2 x 1200	0.70''	...
1122 "Bright" 1	2 x 1750	0.65''	...

found that "faint" masks could not be observed in these conditions.

For the second night (MJD 53788) we concentrated on the "bright" masks only from both fields-of-view. The weather improved significantly together with the 'seeing' which remained $\leq 1''$. During the first part of the second night there was a target-of-opportunity (TOO) that interrupted the first observation. Therefore the 1122 "Bright" 1 mask was observed again in service-mode. Two exposures of 1750 seconds each were carried out in good conditions for each bright mask. The data we were able to observe over three nights is summarised in Table 2.

2.3 Data reduction of the FORS2 data set

At the time of reduction no ESO pipeline existed for the automatic reduction of FORS2 MXU data, so the extraction of galaxy spectra was mainly performed using IRAF with predominant use of the IMUTIL and NOAO packages.

The science frames were stacked to remove contamination by cosmic rays. The majority of these were removed using COSMICRAYS from the CRUTIL package. Significant cosmic rays persisted in regions with strong emission features. Any spurious feature that made it to the final 1-D extraction could later be identified and removed by interpolation.

Each science exposure together with a flat and an arc frame were then sent to a generic spectroscopy reduction pipeline written by D. Kelson (Kelson 2003).²

This software divided the science images containing the 2D spectra by a master flat. The 2D spectra were then rectified to correct for any distortion along the spatial and dispersion axes. Using a He-Ar arc frame the programme found the dispersion relation and wavelength calibrated the 2D spectra. The calibrated 2-D science frame output from the

Kelson software was then sent to the APALL programme in IRAF which performed a variance weighted extraction.

The output of APALL for each slit were 4 1-dimensional arrays: The weighted object spectrum, the unweighted object spectrum, the subtracted sky background and a variance spectrum, all as a function of wavelength.

Spectra were then flux calibrated using the IRAF tasks STANDARD and SENSFUNC. The standard star data was taken by ESO on the night of the observations.

2.3.1 Identification of emission lines

The plotting package SPLOT was used to identify emission lines by eye in the 1-D spectra.

Upon successful identification of any spectral features the galaxy was sent to the NOAO programme RVIDLINES. Each emission line was fitted with a Gaussian profile that was centred on the emission peak. The FWHM of the profile was set to a default 4 pixels (9.72 Å), with a 5 pixel minimum gap between 2 features.

A variance weighted mean redshift was then computed using all of the features identified. The heliocentric correction was made to the redshift using the header information. An RMS error in the redshift was also calculated using the redshift of each feature z_{feature} and \bar{z} in equation (1).

$$\sigma_z = \sqrt{\frac{\sum_{i=1}^n (z_{\text{feature}} - \bar{z})^2}{n - 1}} \quad (1)$$

Figure 2 shows a typical spectrum of a galaxy where only [O II] emission was used to determine the redshift. H β and [O III] lines were lost in the noise. The '4000 Angstrom break' in the SED helped to identify this line as [O II] emission and not H α .

Using this method the redshifts of 180 emission-line dominated galaxies were found.

2.3.2 Identification of absorption lines

Poor signal-to-noise (S/N) meant identifying the redshifts of absorption-dominated galaxies was not possible by inspection. Instead the IRAF programme XCSAO was used (Kurtz & Mink 1998). Absorption features were identified by cross-correlating with a template absorption spectrum. These absorption lines were then used in RVIDLINES to measure redshifts for the 13 absorption-line dominated galaxies that were included in the final table.

2.3.3 Redshift Confidence of the Galaxies

Each of the 193 galaxies that made up the final table were then assigned a redshift confidence level based on the number and strength of any features. The criteria for each level are shown in Table 3.

Those galaxies with a ranking of 1 were most often AGN. The galaxies dominated by absorption lines were assigned a ranking of 2 or 3 depending on how visible the lines were after being identified in XCSAO. 61 confident redshifts were found, even though only [O II] emission was visible because of features such as the '4000 Angstrom break'.

The 28 [O II] emission lines for which there was no alternative feature could have been H α . This meant there

² D. Kelson, The Observatories, Carnegie Institute of Washington, 813 Santa Barbara Street Pasadena, California 91101 USA.

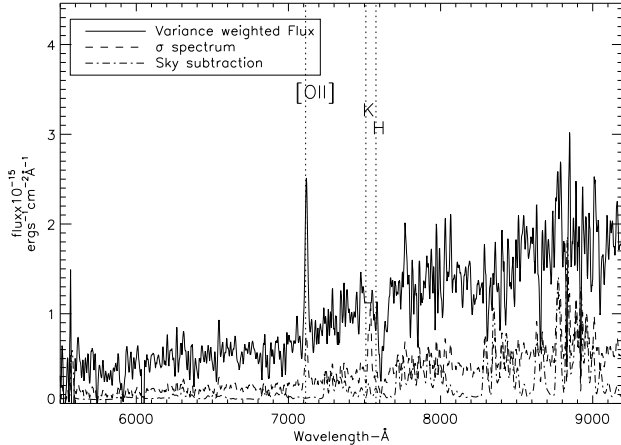


Figure 2. A variance weighted combined spectrum of slit 36 from “bright” mask 1 of sightline HE 1122-1648. The redshift of this emission line dominated galaxy was determined using the [O II] emission line only. The H and K absorption lines were located near a cosmic ray which has been interpolated over at ~ 7500 Å. The feature at ~ 7600 Å is atmospheric O₂ absorption. For display purposes the spectrum has also been box-car smoothed with a window of 5 pixels. The residuals at $\gtrsim 9000$ Å are a product of poor sky-subtraction and so the H β and [O III] doublet could not be identified. The increase in flux above 7600 Å meant the emission line could be identified as [O II] rather than H α because of the ‘4000 Angstrom break’. The σ -spectrum (dashed) and sky value (dot-dashes) that was subtracted are also shown. The value of the sky spectrum has been divided by 100.

Table 3. Confidence levels and criteria needed for the galactic redshifts

Confidence Level	Comment	No. of Galaxies
1	2 or more strong lines	54
2	2 or more moderate lines	26
3	2 or more weak lines	18
4	Secure single line [O II] redshift	61
5	2 or more weak lines from poor spectra	6
6	Ambiguous single line [O II] redshift	28

were a total of 34 spectra (those ranked 5 or 6) for which there were ambiguous results. Figure 3 shows the redshift distribution of the 193 galaxies binned according to whether the redshift was judged to be reliable.

Those galaxies with an insecure redshift were flagged when passed to the code and removed from the calculation. The 61 galaxies only showing confirmed [O II] emission were also flagged in order that they too could be removed in case they significantly changed the result of the correlation.

Being restricted to effectively a single night’s observation meant we did not achieve a large completeness in the galaxy survey. Figure 4 shows the percentage of galaxies with a determined redshift of the 1062 and 1122 objects found using SExtractor. They have been plotted as a function of their separation from the quasar sightline. This incompleteness is accounted for in the calculation of the correlation function.

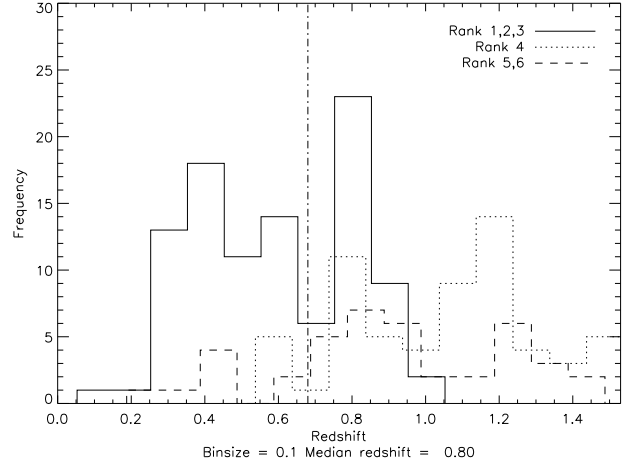


Figure 3. The redshift distribution of the 193 galaxies is shown in this figure, binned as a function of the redshift confidence. This plot shows that most of the galaxies in the galaxy sample used in the correlation were obtained from single line [O II] emission and had a redshift $z_i > 0.8$. The dashed-dotted line at $z = 0.68$ shows the minimum redshift at which galaxies could correlate with Ly- α absorbers found in STIS E230M spectra.

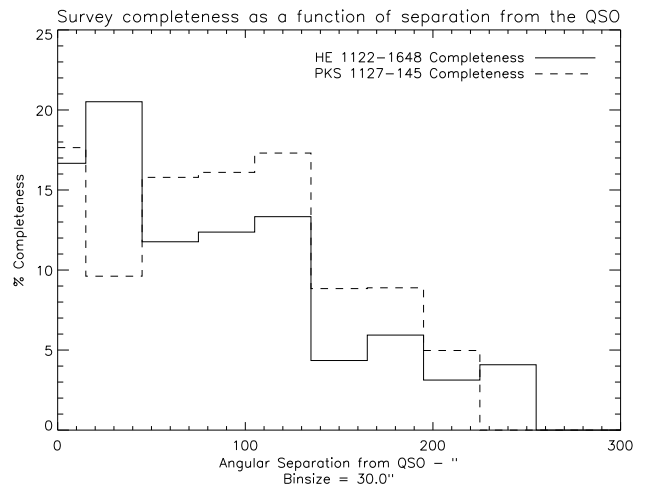


Figure 4. Of the 1062 and 1122 candidate galaxies detected in the fields of quasars HE 1122-1648 and PKS 1127-145 this plot shows the percentage of those with a determined redshift. The completeness is calculated for the apparent magnitude ranges $21.5 \leq m_R \leq 23.0$ and $21.5 \leq m_R \leq 24.5$.

2.4 The Luminosity Distance and K-Correction

Using the selected Λ CDM cosmology stated in Section 1 the luminosity distance to each galaxy (D_L) was found and the absolute magnitude M_B of each galaxy was computed.

$$M_B = m_R - 5 \log_{10} \left(\frac{D_L(z)}{10 \text{ pc}} \right) + K_{\text{correct}} \quad (2)$$

m_R took the value of MAG AUTO that was computed when SExtractor was run on the pre-imaging. As the pre-imaging was only exposed through the red Bessel filter a theoretical K-correction had to be computed using the response curves of two filters and the spectral energy distri-

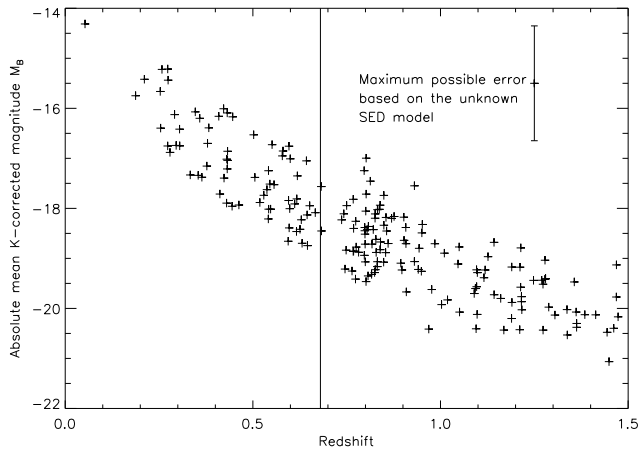


Figure 5. The mean absolute magnitude M_B of the 193 galaxies based on the 5 Bruzual & Charlot (2003) SED templates. The error bar is equal to the largest range in the possible values of M_B from all of the galaxies. The vertical line shows the cut-off at $z = 0.68$ above which the galaxies were at an appropriate redshift to correlate with the Ly- α absorbers and for use in the auto-correlation.

butions (SEDs) of template galaxies. Details of the code used for the colour correction and the template SEDs are described in Bruzual & Charlot (2003).

To compute the $B-R$ K-correction for each spectral type the theoretical flux that would be transmitted through the rest-frame B filter was computed. Each SED was then transformed to a higher redshift in steps of $\Delta z = 0.005$ and the flux through the red filter was integrated. The output from the code was a table, with a value for the K-correction listed as a function of redshift and spectral type. Galactic evolution was not taken into account when transforming the SEDs. With no clear indication from the galaxy spectra as to the spectral type of each galaxy the $B-R$ colours for all 5 templates were considered. Figure 5 shows the mean absolute magnitude of all 193 galaxies based on the 5 SED templates. From Figure 5 it is apparent that we were calculating the cross-correlation and galaxy auto-correlation using galaxies that had $-17 \gtrsim M_B \gtrsim -21$. We did not have a sufficient number of galaxies to investigate the dependence of the correlation on the galaxy magnitudes.

Altogether the spectroscopic redshifts of 193 galaxies were found and were added to a master catalogue. This included 37 in the field of HE 1122-1648 that were at a redshift of $z \geq 0.68$ and had a redshift confidence ≤ 4 , and so could be correlated with the Ly- α absorbers. The number of galaxies that could be used in the calculation that were found in the field of PKS 1127-145 was 58.

3 QUASAR UV SPECTROSCOPY

The Ly- α absorbers used in the cross-correlation function were detected in the absorption spectra of the background quasars HE 1122-1648 and PKS 1127-145. These quasars were selected because high resolution ($R = 30000$), STIS echelle spectroscopy obtained using the E230M grating ex-

Table 4. Spectra from the ESO and HST data archives

Instrument + grating	λ (\AA)	Exp time (s)	$\frac{\lambda}{\Delta\lambda}$
HE 1122-1648			
STIS E230M ^a	2270-3111	4x2877	30000
STIS E230M ^a	1574-2382	6x2712	30000
STIS G430L ^a	2900-5700	2x1000	1040
FOS G190H ^b	1571-2311	3x1873	1300
UVES Blue/Red ^c	3200-5765	15x5400	45000
PKS 1127-145			
STIS E230M ^d	2270-3111	14x5798	30000
FOS G190H ^e	1571-2311	4x2160	1300
FOS G160L ^f	901-2508	1x1450	250
UVES Blue/Red ^g	3200-6809	10X3060+4x4800	45000

a) PI Baldwin HST proposal 9885 b) PI Reimers HST proposal 5950 c) Schaye et al. (2007); Kim et al. (2002) d) PI Bechtold HST proposal 9173 e) Deharveng et al. (1995) f) Pettini et al. (1999) g) Kacprzak et al. (2007)

ists within the HST archive. These archived spectra cover the wavelength range 2050-3111 \AA , the range of wavelengths needed to locate Ly- α lines at a redshift of $z \sim 1$. With such a high dispersion, it was hoped that low column density ($\log_{10}(N_{\text{HI}}(\text{cm}^{-2})) \sim 13$) HI absorption lines could be resolved and Voigt profiles fitted in order that their column density and b-parameter could be determined.

The absorber sample in this paper has a higher resolution than the absorber data set of Morris & Jannuzi (2006). They used HST FOS data and a fitted b-parameter that was fixed at 30 km s^{-1} . The STIS E230M instrumental broadening was 10 km s^{-1} in the spectra we used, compared to 230 km s^{-1} for FOS spectra. Therefore in principle we are sensitive to lower column density lines than Morris & Jannuzi (2006), and we can directly measure the b-parameters for absorbers, rather than assuming a value of 30 km s^{-1} .

The only Ly- α absorbers that were used in the correlation function were detected using the Space-Telescope-Imaging-Spectrograph (STIS) in echelle mode with the E230M grating. In addition to these, to help identify lines and to compile a more complete line-list, spectra were analysed that were taken by STIS in long-slit mode, the low-resolution Faint Object Spectrograph (FOS) and the ESO UVES (Ultraviolet and Visual Echelle Spectrograph) instrument.

Table 4 lists the data products used in the investigation that were collected from the STScI (Space Telescope Science Institute) and ESO (European Southern Observatory) archives (Keyes et al. 1995; Kim Quijano et al. 2007; Kaufer et al. 2007).

3.1 Reduction of both long-slit and echelle spectra

The preliminary calibration and reduction of data for each instrument was performed by STScI or ESO ‘on-the-fly’ by an instrument specific pipeline. The steps performed in the initial reduction of raw data depended on the detector.

3.1.1 FOS calibration

The details for the FOS pipeline CALFOS are from Keyes et al. (1995) and they differed significantly from both the STIS and UVES pipelines as the data was already 1-dimensional. The pipeline began by computing the statistical error in the raw data, this was then carried forward through each reduction step and used in the variance spectrum. The total photon count was divided by the exposure time to give the count rate. Next the background sources of noise were subtracted. This included the dark current generated by the instrument and scattered light from the optics. The variations in sensitivity with λ from diode-to-diode and the illumination correction were then compensated for by dividing each pixel by the flat-field response. After each observation FOS would perform an arc exposure using the internal Pt-Cr-Ne lamp in order to find the wavelength zero-point. Vacuum wavelengths were used and the pipeline, using the date of observation, performed a heliocentric velocity correction. Finally using the data from a spectrophotometric star the pipeline flux calibrated the object spectrum converting the count rate to $\text{ergs s}^{-1} \text{cm}^{-2} \text{\AA}^{-1}$, thereby correcting for the telescope and spectrograph transmission and the detector efficiency.

3.1.2 STIS calibration

The initial stage of the pipeline CALSTIS varied depending on whether the data was taken using the MAMA or CCD detector. A detailed description of both pipelines is covered in Kim Quijano et al. (2007). Similar to the FOS pipeline the first process was to calculate a statistical error, this error was then propagated through the reduction pipeline. The dark current was then subtracted and the 2D spectra were divided by a flat field exposure created by a lamp within the spectrograph. The STIS CCD data was reduced in the same manner as generic CCD optical data. For both UV and optical data the STIS pipeline then used an arc exposure to calculate the wavelength dispersion solution with the necessary heliocentric velocity correction. Using a spectrophotometric star the spectra were also flux calibrated to give counts in $\text{ergs s}^{-1} \text{cm}^{-2} \text{\AA}^{-1}$. The 2D long-slit and echelle data were then binned along the spatial axis to produce 1D spectra.

3.1.3 UVES Calibration

The pipeline steps for the UVES raw data followed the same procedure as the STIS optical data save for two main differences. As UVES is a ground based instrument the sky needed to be subtracted when extracting the 1D spectra.

When we analysed the absorption lines of the UVES spectra we used vacuum wavelengths so that they would correspond to the absorption lines of the STIS data. Therefore the dispersion solution needed to undergo an air-to-vacuum wavelength correction before transforming to the heliocentric reference frame.

3.1.4 Combining multiple exposures

We performed the final steps in reducing the 1D spectra. We combined exposures using variance weighting and fitting a

QSO continuum. A different method was used depending on whether the spectrum was long-slit data or from echelle spectroscopy.

The nature of digicon, MAMA and CCD detectors means that, prior to any combining of exposures, each of the spectra had a wavelength relation that was not the same or constant as $\Delta\lambda \propto \lambda$. So the first step before combining multiple exposures was to inspect their dispersion and then re-sample each of the spectra to a common wavelength solution.

3.1.5 Fitting the QSO continuum

When analysing absorption lines the QSO flux needed to be divided by the QSO continuum.

The continua for the long-slit spectra were fit using the IRAF programme SPLOT. The first step when estimating a continuum was to crop the spectrum by $\sim 100 \text{\AA}$ at both the red and blue ends. This was to remove data with a S/N per pixel ≤ 2 . Any emission features or large absorption profiles were also clipped. In particular this included the Ly- α and Ly- β emission lines if they were present. The continuum of a QSO spectrum was fitted by sampling the spectrum at points devoid of absorption, usually in regions redwards of the Ly- α emission, this was then extrapolated to lower wavelengths. A chebyshev function of order 2 was fit to the data using SPLOT. The final spectra were then saved in a FITS format for use in RDGEN, a programme that would normalise the spectra by dividing through by the continuum and detect absorption features. RDGEN is part of the VP-FIT³ package that was used when modelling Voigt profiles.

3.2 Post calibration STIS E230M and UVES Echelle spectroscopy reduction

The echelle data was composed of many exposures, these not only needed to be re-sampled and combined, but also the separate overlapping orders needed to be joined end-to-end while simultaneously avoiding aliasing or losing flux when re-sampling. For this reason a C program called UVES popler (version 0.17) (Murphy et al. 2007) was used. This was devised and written by M. T. Murphy⁴ with the intention of reducing post-pipeline UVES echelle data. The input for UVES popler were all the optimally extracted echelle orders from the STScI CALSTIS and UVES pipeline and the associated variance spectra. Combining these orders, resampling the data, setting a common dispersion solution and normalising by the QSO continuum was then an automated process.

Parameters were passed to UVES popler that gave the function and order to fit for the continuum. A chebyshev function of order 2 was selected above and below the Ly- α emission line. High column density absorption lines were ignored by UVES popler by rejecting any data that was in the lower 50% of the flux values below the Ly- α emission line.

³ ©2007 R.F.Carswell, J.K. Webb, M.J. Irwin, A.J. Cooke, Institute of Astronomy, Madingley Rd, Cambridge, CB3 0HA, Uk.

⁴ M. Murphy, Centre for Astrophysics & Supercomputing, Swinburne University of Technology, Mail 39, PO Box 218, Hawthorn, Victoria 3122, Australia

Flux values that made up the lower 30% of the data above Ly- α were also ignored. A higher tolerance was permitted at these wavelengths as there were only a few metal absorption lines and no forest absorption.

The level to set the continuum was then iteratively improved by neglecting data that remained 1.2σ below a provisional continuum line and any emission/noise features that existed 3σ above. We visually inspected the final continuum, adjusting it by hand where necessary. Errors in the continuum level may introduce small errors in the inferred column densities of lines for regions of our spectrum with low S/N (≤ 3), but we do not expect these errors to affect our measurement of the line redshifts.

Both HE 1122-1648 and PKS 1127-145 were fit with the same parameters for the STIS and UVES spectra.

3.3 Producing a Quasar Absorption line-list

Locating the Ly- α absorbers that would be used in the cross-correlation function at a redshift $z \sim 1$ required the STIS E230M data. The other spectra were used for completeness, for the identification of metals and to corroborate the identity of STIS Ly- α absorption lines.

The Ly- α and Ly- β emission lines of quasar PKS 1127-145 are located at 2658.67 Å and 2243.25 Å. Therefore only the Ly- α series lines were within the wavelength range of the E230M data. Ly- α , Ly- β and Ly- γ emission lines for quasar HE 1122-1648 were at 4133.28 Å, 3487.46 Å and 3229.13 Å respectively. Hence many Lyman series absorptions were located in the UVES and STIS spectra. Locating these lines first was essential so that higher order Lyman lines could be identified and removed. Any remaining lines could then only be Ly- α absorptions (or metals).

We used RDGEN to locate absorption lines. Using the velocity FWHM of the instruments; that were 10.0 km s^{-1} , 6.7 km s^{-1} and 230 km s^{-1} for the STIS E230M, UVES and FOS G190H gratings respectively. The output from this was a table that included the wavelength, the observed equivalent width (EW), the error associated with these parameters and the significance of the absorption line.

The significance level of each line was defined as, given error in the EW σ_{EW} .

$$SL = \frac{EW}{\sigma_{EW}} \quad (3)$$

At this stage all the lines within the STIS spectra where RDGEN had estimated an EW significance $\sigma \geq 3$ were passed forward to the line-fitting programme VPFIT. No contribution to the error in the EW caused by the error in the level of the continuum was included at this point.

Absorption lines were fitted with Voigt profiles using VPFIT (version 9.3). Using the instrumental velocity FWHM VPFIT would attempt to model the absorption line. This was achieved by a χ^2 minimisation when comparing the data and fitted Voigt profiles. The parameters of the lines were then returned together with 1σ errors. The input to the programme was a table of the absorbers detected using RDGEN that included the ion species and an approximate initial guess for the redshift, column density and b-parameter. The atomic data required was taken from Morton (2003).

The following steps were made when identifying and then modelling the lines. First the galactic lines such as Mg II

and Fe II were identified and flagged as any redshifted line that was blended with these had to be ignored.

The second step was to identify redshifted metal lines above the Ly- α emission line. No redshifted metal lines were detected at any wavelength in the STIS spectra. Those detected in UVES were associated with a damped ($\log_{10}(N_{\text{HI}}(\text{cm}^{-2})) \geq 20$) system. The HE 1122-1648 FOS G190H data exhibited a damped system at $z = 0.681$ ($\log_{10}(N_{\text{HI}}(\text{cm}^{-2})) = 20.5 \pm 0.03$). C IV, Mg II and Fe II absorption lines located in the UVES spectrum are associated with this.

The other method employed to identify metal lines such as C IV and Mg II was by their doublet wavelength separation.

Metal lines were found within the Lyman-series forest, in particular the doublets C IV ($\lambda\lambda 1548.20, 1550.77$) and O VI ($\lambda\lambda 1031.93, 1037.62$). As this was done by eye only two ways were known to discriminate between metals and possible Ly- α lines. First if both lines could be spotted there was the doublet spacing. In addition, for metal lines the b-parameter is usually $\leq 10 \text{ km s}^{-1}$ while for Ly- α b it is seldom $\leq 15 \text{ km s}^{-1}$ and cannot be $< 10 \text{ km s}^{-1}$ (Janknecht et al. 2006). So an inspection of the FWHM gave a good indication as to the nature of the species.

With the metal absorption lines identified it could now be assumed that those left were Lyman lines. First of all, any remaining unidentified lines within the Ly- α forest were assumed to be HI. RDGEN was then used to plot the output of VPFIT and the location of the Ly- β lines were highlighted. VPFIT was then rerun if there was a positive match so that both lines could be used to constrain the errors. Any line remaining unidentified within the Ly- β forest could only then be Ly- α . This process was repeated towards shorter wavelengths until the blue end of the STIS echelle spectrum was reached. In the case of PKS 1127-145 only the Ly- α forest was visible. The damped system at $z = 0.681$ in the HE 1122-1648 spectrum prevented any further lines being discovered at shorter wavelengths.

3.3.1 The minimum detectable column density

An effective way to decide the minimum detectable EW for the Ly- α lines was to invert the spectrum around the continuum, and using the b value of the smallest real Ly- α absorber we attempted to fit an ‘absorption line’ to the inverted spectrum. A line that we knew was a sample of the noise. When the column density and 1σ error to the largest noise profile became indistinguishable from that of the smallest known real absorber this gave the minimum reliable value. For the PKS1127-145 and HE 1122-1648 STIS spectra the minimum detectable column densities were $\log_{10}(N_{\text{HI}}(\text{cm}^{-2})) = 13.2$ and $\log_{10}(N_{\text{HI}}(\text{cm}^{-2})) = 13.5$ respectively. For the UVES HE 1122-1648 spectrum where the S/N was $\sim 120 \text{ pixel}^{-1}$ at the central wavelength (Dall’Aglio et al. 2008) this minimum decreased to $\log_{10}(N_{\text{HI}}(\text{cm}^{-2})) = 11.7$.

VPFIT would sometimes attempt to fit these weak lines with unphysical b-parameters. As the Doppler parameter is $\propto \sqrt{\frac{2kT}{m}}$ any Ly- α line that was fitted with $b \leq 10 \text{ km s}^{-1}$ was dropped from the list, where we have adopted the same cut that was used in Janknecht et al. (2006).

3.4 Extracting lines from data with very poor signal-to-noise

3.4.1 Fixing the variables

We set VPFIT to terminate if the 1σ error in the column density was greater than $\Delta\log_{10}(N_{\text{HI}}(\text{cm}^{-2})) = 0.5$. Whenever this point was reached we would fix the b-parameter to the median b value of those lines that had been measured. This was 26.5 km s^{-1} . This was done for all of the Ly- α lines below 2300 \AA regardless of $\Delta\log(N_{\text{HI}})$ in the HE 1122-1648 STIS spectrum where the S/N was very poor.

3.4.2 The blue HE 1122-1648 STIS E230M spectrum

The S/N of this spectrum was below 2 for most wavelengths. The wavelength range was meant to cover $1574 \rightarrow 2382 \text{ \AA}$ but the data became unusable below the damped system at 2050 \AA .

In an effort to recover the absorption features in this low S/N data, we summed the flux over a narrow bandpass of 24 pixels and then plotted this as a function of wavelength. The wavelength of the absorption lines that were lost unbinned data could then be determined. Knowing where these lines were meant that Voigt profiles of a fixed b-parameter could then be fit.

The spectrum was cropped to remove those wavelengths below the DLA Ly- α line. The flux absorbed (d_i) per pixel i was then summed over a window of size $M+1$ using the following calculation. C_i is the continuum level normalised to 1 for all i and F_i is the flux.

$$d_i = \sum_{j=-\frac{M}{2}}^{\frac{M}{2}-1} (C_{i+j} - F_{i+j}) \times (\lambda_{i+j+1} - \lambda_{i+j}) \quad (4)$$

The variance of this result was also computed where the values were summed in quadrature.

$$\sigma_i = \sqrt{\sum_{j=-\frac{M}{2}}^{\frac{M}{2}-1} [\sigma_{i+j} (\lambda_{i+j+1} - \lambda_{i+j})]^2} \quad (5)$$

The summed absorbed flux as a function of wavelength is plotted in Figure 6a.

Two identifications were made in this spectrum. These were two Ly- β lines associated with the systems at $z = 1.229$ and $z = 1.234$, these can be seen in Figure 6a at $\sim 2290 \text{ \AA}$. The smallest profile had a width of 24 pixels, so assuming this profile which had an EW significance $\sigma = 8.7$, was typical of the minimum width we could hope to identify, this was chosen to be the window size M .

The next variable to find was the minimum detectable EW for a line. For this we adapted the earlier method of inverting the spectrum to sample the noise. Equation (4) was applied to the inverted spectrum using the same window size, this is plotted in Figure 6b. The peak inverted summed ‘flux’ had a value of 0.54. Using this cut on the real summed spectrum meant only 28 absorbers would be included. So by using the peak noise value there was a danger that many real Ly- α absorbers would be lost.

The red HE 1122-1648 STIS E230M spectrum had a Ly- α line density of $\frac{dN}{dz} = 198$ and all results indicate that

the line density distribution is almost flat at redshifts $z \leq 1$ (Kirkman et al. 2007), so a similar value is expected. The conservative cut that left 28 absorbers implied a line density of $\frac{dN}{dz} = 165$. This cut-off needed to be reduced by 20% to a minimum flux-deficit of 0.43 before a similar line density could be observed. Figure 6b shows such a minimum cut-off would allow a lot of false identifications from smoothed noise.

Therefore the cut was varied between 0.43 and 0.54 in order to see to what proportion of lines would be excluded when compared to the density of Ly- α lines that are expected. Eventually the cut-off in Figure 6b was set to exclude all but the highest noise peaks at 0.49. In doing this 46 absorbers were identified. A programme was then written that measured the wavelength of these peaks. Those that were higher order HI lines or had an EW significance less than 3 were removed. This left 31 Ly- α absorbers that could be measured using VPFIT.

The original flux and variance spectra were then smoothed using a box-car window of 11 pixels and this was used in the VPFIT programme. VPFIT was now successful in modelling the Voigt profiles with 1σ errors in the column density $\Delta\log_{10}(N_{\text{HI}}(\text{cm}^{-2})) < 0.5$ and these absorbers were added to the final line-list. All of the lines found using this method had a b-parameter fixed to the median value found for those lines that had been fitted successfully at higher wavelengths of 26.5 km s^{-1} .

3.5 Variance Weighted Equivalent Width Significance and the Continuum error

All Ly- α lines with an equivalent width significance $SL \geq 3$ were included in the cross-correlation function, this is the level adopted in Schneider et al. (1993). However we had to fix the b-parameter for 42 out of the 135 Ly- α lines in the STIS spectra that had an equivalent width significance of 3, and assume the continuum was correct. Therefore the EW and significance of the lines were measured again. This time a Gaussian weighting was used where changes in the significance of a line because of errors in the continuum were also considered. The formulae used to calculate the EW and significance have been adapted from Schneider et al. (1993).

Consider an absorption line that covers J pixels and is centred on pixel i with the continuum C set to 1. The EW of the profile is equal to:

$$EW = \frac{\Delta\lambda_i \sum_{j=1}^{j=J} \eta_j (C_{i+j-J/2} - F_{i+j-J/2})}{\sum_{j=1}^{j=J} \eta_j^2} \quad (6)$$

$\Delta\lambda_i$ was assumed to be constant across the absorption, and η_j is the Gaussian weighting coefficient where $\sum_{j=1}^{j=J} \eta_j = 1$. The FWHM of the Gaussian profile for each absorber was based on its b-parameter.

The amount that the variance spectrum (σ^2) contributed to the error in the EW was computed using:

$$\delta(EW_{\text{var}}) = \frac{\Delta\lambda_i \sqrt{\sum_{j=1}^{j=J} \eta_j^2 \sigma_j^2}}{\sum_{j=1}^{j=J} \eta_j^2} \quad (7)$$

The significance of each line was then, like equation (3), the ratio of equations (6) and (7).

Our approach when testing the effect of changes in the

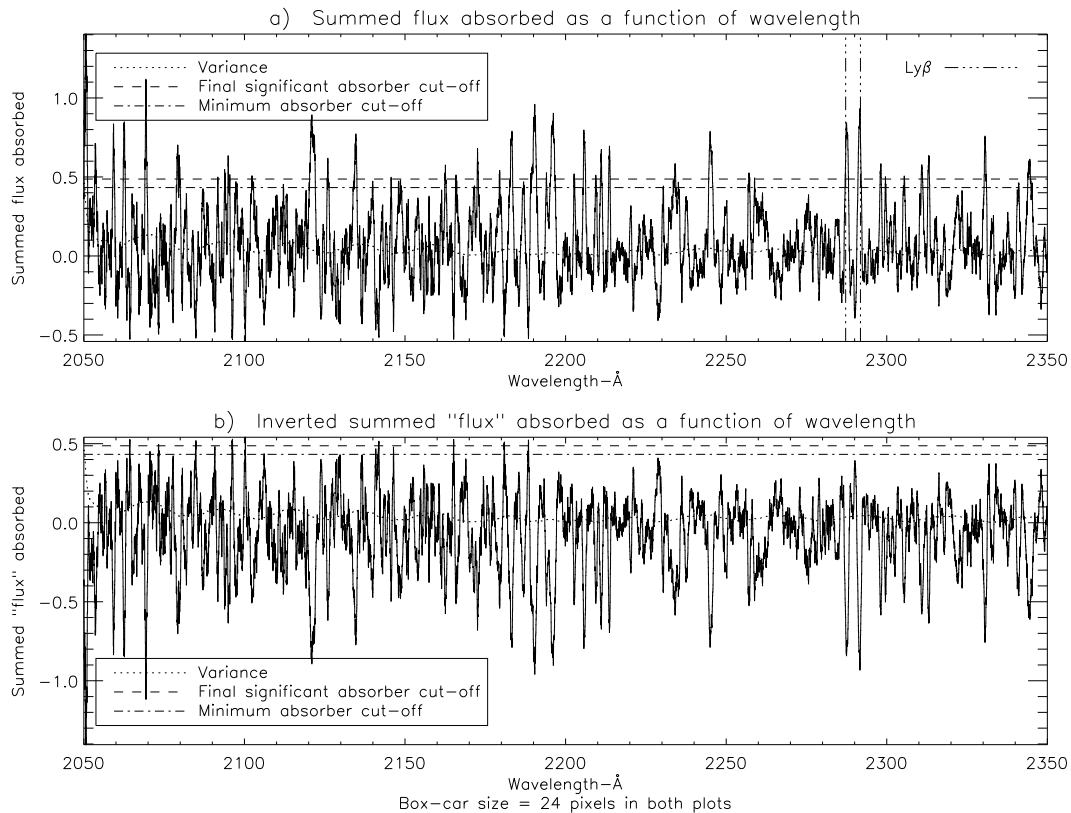


Figure 6. (a) In order to locate Ly- α absorbers in the blue STIS E230M spectrum of HE 1122-1648 the absorbed flux was summed over a window of 24 pixels using equation (4). This way any absorbers were enhanced and could be modelled using VPFIT. (b) The ‘significant absorber’ cut-off lines were set by inverting about the continuum the spectrum and sampling the noise. To recover the expected line-density at this redshift would require a cut in the flux deficit of 0.43, however many noise features would then be included (dashed-dot line). Thus a more conservative cut of 0.49 was chosen. After a final EW significance level cut $SL \geq 3$ 31 Ly- α lines were identified.

level of the continuum was to estimate the significance levels when an error $\delta(C_j - F_j)$ of 10% was added. VPFIT was not rerun to find new values for the b-parameter or the column density.

$$(\delta EW_{j \text{ cont}})^2 = \left(\frac{\partial EW_j}{\partial (C_j - F_j)} \right)^2 (\delta (C_j - F_j))^2 \quad (8a)$$

$$\therefore (\delta EW_{\text{cont}})^2 = \sum_{j=1}^J \left(\frac{\Delta \lambda_i \eta_j}{\sum_{j=1}^J \eta_j^2} \right)^2 \times 0.01 \quad (8b)$$

Errors in the EW, that included contributions from both the continuum and variance, were calculated using equations (7) and (8b) summed in quadrature. Those absorbers that had a new variance weighted equivalent width significance $\sigma \geq 3$ were used in the cross-correlation.

It was found that even with a 10% error margin in the continuum, the Gaussian weighted significance of all the STIS absorption lines did not change by more than 1% and no additional lines were lost because of the 3σ cut. This was because of the relatively high minimum observable optical depth produced by a Ly- α column density of $\log_{10}(N_{\text{HI}}(\text{cm}^{-2})) = 13.2$.

Figure 7 shows the EW of the 135 lines detected in the STIS spectra that had a significance level ≥ 3 .

One can observe that the peak in the redshift distribution of galaxies in Figure 3 is at redshifts $z \sim 0.8$. Thus many of the pairs in the correlation according to Figure 7 were

made with those absorbers from the spectrum with poor S/N. These are absorbers with a higher minimum EW limit hence a lower completeness. Pairs from this region made up 72 of the 171 detected in the cross-correlation plot in Figure 12a. The effect of this increase in the minimum EW means we may over-estimate the cross-correlation. It is absorbers with a small EW that also have a low column density, and we do not expect any correlation with absorbers that have $\log_{10}(N_{\text{HI}}(\text{cm}^{-2})) \leq 13.5$ (Chen & Mulchaey 2009).

3.6 The Final line-lists

The final line-list for HE 1122-1648 contained 740 absorption lines that were detected in the STIS E230M and UVES echelle data that had an equivalent width significance greater than 3. This included 586 Ly- α lines each with a b-parameter $\geq 10 \text{ km s}^{-1}$ and 154 metals. Of these Ly- α lines 97 came from the two STIS E230M spectra.

Fewer Ly- α lines were detected in the STIS spectrum of PKS 1127-145 due to the lower quasar redshift. 38 Ly- α lines were found together with 23 metal lines in both the STIS and UVES spectra. Therefore over a total path length of $\Delta z = 1.08$ we detected 135 Ly- α absorbers that could be used in the correlation function.

The minimum column density for the Ly- α absorbers used in the correlation function was $\log_{10}(N_{\text{HI}}(\text{cm}^{-2})) =$

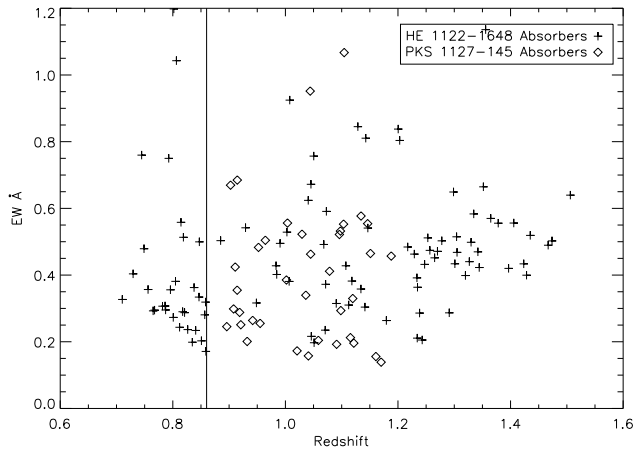


Figure 7. The equivalent width of those Ly- α absorbers with a significance $\sigma \geq 3$ as a function of redshift. The increasing minimum detectable EW of those absorbers from opposite ends of the HE 1122-1648 STIS spectrum can be observed. Those absorbers below the vertical line at $z = 0.86$ were detected in the low S/N blue STIS spectrum.

13.2. The maximum column density detected was $\log_{10}(N_{\text{HI}}(\text{cm}^{-2})) = 17.4$, however only 11 absorbers out of those correlated had a column density greater than $\log_{10}(N_{\text{HI}}(\text{cm}^{-2})) = 15$. The median column density was $\log_{10}(N_{\text{HI}}(\text{cm}^{-2})) = 14.0$. The complete line-lists for both HE 1122-1648 and PKS 1127-145 are available in electronic format.

4 THE 2-POINT CROSS-CORRELATION FUNCTION

When investigating the relationship between gas and galaxies the calculation for the 2D 2-point correlation was based on the estimator devised by Davis & Peebles (1983). The 2D 2-point correlation function ($\xi_{\text{AG}}(\sigma, \pi)$) in equation (9) gives the measure of association between the Ly- α absorbers and galaxies across both the projected (σ) and line of sight (π) separations by comparing the real distribution of pairs with random catalogues.

$$\xi_{\text{AG}}(\sigma, \pi) = N_{\text{QSO}} \frac{\text{DD}}{\text{RR}} - 1 \quad (9)$$

Along each line of sight every absorber was paired with every galaxy and the impact parameter and line of sight separation in co-moving coordinates was calculated for each pair. Each random absorber was also paired with every random galaxy and the separation found between these pairs. DD and RR are the number of real-real and random-random pairs respectively in each bin along the π and σ separations.

The normalisation constant N_{QSO} fixed the total number of random pairs to the same value as the number of real pairs across all σ and π . This way $\xi_{\text{AG}}(\sigma, \pi)$ gave a value for the fractional excess of pairs compared to a random distribution. Due to the different number of real pairs that occur along each quasar sightline a separate normalisation

constant was calculated for each field before the pairs were binned together.

To compare the values of ξ_{AG} against a known observable the galaxy auto-correlation function ξ_{GG} was calculated using the same techniques as the cross-correlation.

4.1 Measuring separations

The line of sight co-moving distance (D_{C}), to both galaxies and absorbers that are at a redshift z , was calculated using equation (10).

$$D_{\text{C}} = \frac{c}{H_0} \int_0^z \frac{dz'}{\sqrt{\Omega_{\text{M}}(1+z')^3 + \Omega_{\Lambda}}} \quad (10)$$

The line of sight separation, π , was then $\pi = |D_{\text{C galax}} - D_{\text{C absorber}}|$.

The angular separation between 2 points on an image that have been projected from the celestial sphere is given by equation (11), where δ and α are the declination and R.A. of the targets in radians.

$$D_{\angle} = \arccos(\sin \delta_{\text{abs}} \sin \delta_{\text{gal}} + \cos \delta_{\text{abs}} \cos \delta_{\text{gal}} \cos(\alpha_{\text{gal}} - \alpha_{\text{abs}})) \quad (11)$$

The RA and DEC of each absorber were the J2000 coordinates of the quasar in question retrieved from the SIMBAD database. Using the mean line of sight distance towards both the absorber and galaxy, the impact parameter was then calculated to be $\sigma = D_{\angle} D_{\text{C}}$. As long as the π separation was $\leq 20 h_{70}^{-1}$ Mpc, each real galaxy-absorber pair was then written out to a file for subsequent binning.

4.2 Generating the random catalogues

4.2.1 The random galaxies

When producing the random catalogues it was important that the random galaxies have the same position on the sky as the data in order to keep the mask design information. Therefore adopting the technique used in W07, each real galaxy that lay in the redshift range of the STIS E230M spectra of that particular line-of-sight was replaced with 200 fake galaxies in that position on the sky.

In order not to bias the 2D correlation function it was also important that the redshift distribution of the random galaxies be the same as the real sample. To achieve this the redshift of each randomly generated galaxy was a perturbation of $\delta z = \pm 0.01 \rightarrow 0.05$ from the galaxy that spawned it. This range was chosen so that no random pair generated from the same real pair would appear within the plotting space of $\Delta\pi = 20.0$, $\Delta\sigma = 5.0 h_{70}^{-1}$ Mpc. For example there are 37 galaxies in the field of HE 1122-1648 between redshifts $z = 0.68 \rightarrow 1.51$, hence there were $37 \times 200 = 7400$ random galaxies.

4.2.2 The random absorbers

The random absorbers were generated in the same fashion. Each real absorber was replaced with 200 randoms, each

with the same column density, b-parameter and EW as the original.

So that the random absorbers would have the same line-density as the real sample, the redshift of each random absorber was also a perturbation from the original. $\delta z = \pm 0.06 \rightarrow 0.1$. The separation between all random absorbers and random galaxies was then collected and likewise binned if $\Delta\pi \leq 20.0 h_{70}^{-1}$ Mpc.

Using 200 random targets per real absorber or galaxy was decided on a trial basis. This value was a compromise between limited computing power and ensuring that the RR pair distributions were sufficiently smooth, with little variation in the number of pairs along the line of sight at separations of equal impact parameter.

4.3 Binning for the 2D plot

We selected pairs separated by less than or equal to 20 and 5 co-moving h_{70}^{-1} Mpc along the π and σ directions respectively and binned them on a grid. Each value in this array was then divided by the equivalent bin in the RR array and 1 subtracted to give $\xi_{AG}(\sigma, \pi)$. Our choice of binning was $\Delta\sigma = 1.0 h_{70}^{-1}$ Mpc, and $\Delta\pi = 2.0 h_{70}^{-1}$ Mpc. This was coarser than the earlier studies of RW06 and W07, who binned $\Delta\pi = \Delta\sigma = 0.1 h_{100}^{-1}$ Mpc and $\Delta\pi = 2.0 \Delta\sigma = 0.4 h_{70}^{-1}$ Mpc. We required this coarser sampling because of the small number of real pairs.

4.4 The error calculation

In the previous studies of RW06 and W07, the uncertainty in ξ was calculated by jackknife resampling of all the sightlines. The correlation function was recalculated removing one quasar at a time and an error determined for each bin.

Having only two quasars in this study an alternative method was chosen where mock galaxy tables and linelists were created with the same number of absorbers and galaxies and redshift distribution as the real data. The generation of mock redshifts was identical to that used to generate the random catalogues described above. These were then treated as real data sets and run using the exact same code. 50 of these mock linelists and galaxy tables were produced together with 50 estimates for the correlation function made by removing one of the mock absorber and galaxy catalogues at a time.⁵ A RMS error based on the sample variance was then calculated using equation (12). With $N = 50$ mock datasets,

$$\sigma_{\xi(\sigma, \pi)} = \sqrt{\frac{\sum_i (\bar{\xi} - \xi_i)^2}{N - 1}} \quad (12)$$

The Poisson error was found to overestimate the significance of the correlation result (W07), and so was not calculated.

⁵ To avoid confusion ‘mock’ catalogues are ones treated as real data in order to estimate an error and all have an independent value for DD. Random catalogues, be they from the real or mock data, are used in the denominator of the estimator.

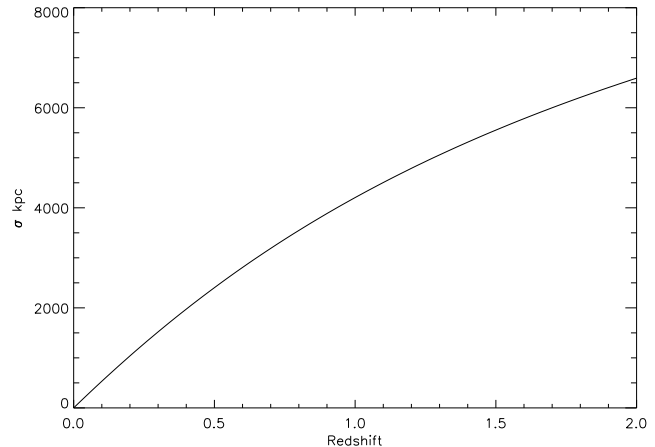


Figure 8. The curve in this diagram shows the increase in the maximum possible observable impact parameter when using the $6.8' \times 5.7'$ detector on the FORS2 instrument. This plot was derived using our stated cosmology and assuming that the galaxy was located in the corner of the detector, the angular separation $\delta\theta^2 = 3.4'^2 + 2.85'^2$ from the QSO at the centre of the chip. The constraints of the size of the field and the maximum galaxy redshift meant we were able to correlate galaxies with absorbers out to a projected distance of $\sigma = 5 h_{70}^{-1}$ Mpc.

5 RESULTS

5.1 The Galaxy Impact Parameter Distribution

The maximum possible impact parameter between Ly- α absorber and galaxy pairs is a function of redshift and was constrained by the $6.8' \times 5.7'$ field of view of the FORS2 detector. Figure 8 shows a plot of the maximum possible impact parameter. The solid line in Figure 9 is a histogram of the projected separation between all 193 galaxies in the survey and the central quasar sightline.

The initial shape is caused by the increase with redshift in the number of galaxies located within each concentric cylinder centred on the quasar.

This distribution then peaked along a plateau at a projected separation of $\sigma = 800 - 2000 h_{70}^{-1}$ kpc before rapidly declining above $\sigma = 3000 h_{70}^{-1}$ kpc. This flattening of the distribution reflects the peaks in the histogram of Figure 3 and the expected range in impact parameter at these redshifts (see Figure 8).

Figure 3 shows most of the galaxies were detected at a redshift $z \sim 0.8$. Therefore the peak in Figure 9 must occur below $\sigma \sim 3000 h_{70}^{-1}$ kpc. The number of galaxies per bin had already started to decline by $\sigma = 2000 h_{70}^{-1}$ kpc. This was caused by a decrease in the radial density of slits as the edge of the rectangular $6.8' \times 5.7'$ detector was reached.

The number of galaxies above $\sigma = 4000 h_{70}^{-1}$ kpc was low because the size of the chip meant that a minimum redshift $z \gtrsim 1$ was required to reach this impact parameter.

The dashed histogram is a completeness test that shows the expected separation had every galaxy within the same magnitude range ($21.5 \leq m_R \leq 24.5$) been targeted. Mock galaxies were placed with a uniform spacing over the same $6.8' \times 5.7'$ area. The required surface density for this magnitude cut came from Figure 4 of Hogg et al. (1997). Each mock galaxy was then assigned a random redshift taken from

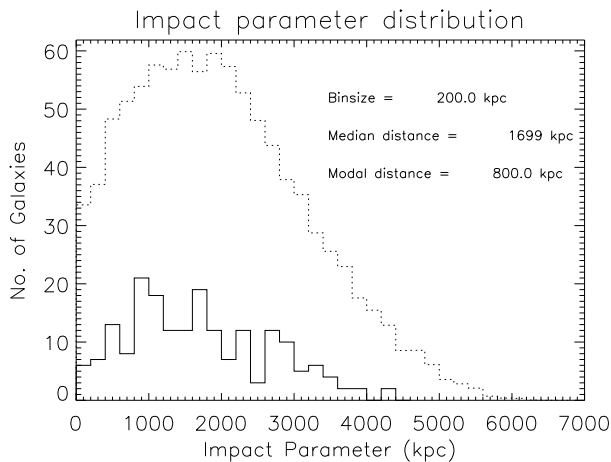


Figure 9. The solid line histogram shows the number of galaxies surveyed as a function of impact parameter binned by $200 h_{70}^{-1}$ kpc. The number of galaxies observed has an expected increase, peaking at $800\text{--}2000 h_{70}^{-1}$ kpc as the survey volume increases. The edge effects of the chip and the drop off in the number of galaxies at high redshift then cause a decrease in the number of galaxies beyond $3000 h_{70}^{-1}$ kpc. The dotted line represents the expected number of galaxies in a complete magnitude limited survey ($21.5 \leq R \leq 24.5$) where the data is from Cohen et al. (2000); Hogg et al. (1997). This plot shows that even though we were able to sample the correct impact distribution for the galaxies the survey was far from complete.

the Hubble Deep Field North Survey redshift distribution from Table 4 of Cohen et al. (2000). A fiducial redshift cut-off for the mock galaxies was chosen to be 1.8. We then calculated the impact parameter of each mock galaxy from an imaginary sight line located at the centre of the CCD. This was repeated using 1000 mock galaxy catalogues in order to calculate the expected impact parameter distribution.

Figure 9 shows that our galaxy survey follows the same general shape as the expected distribution. The mock catalogue also peaks in the range $\sigma \sim 1000 - 2000 h_{70}^{-1}$ kpc before decreasing above $\sigma = 2000 h_{70}^{-1}$ kpc because of edge effects. However the figure also shows that our survey was far from complete.

5.2 The Ly- α Absorber Redshift distribution

Figure 10 shows a histogram of all the Ly- α absorption lines detected with an equivalent width (EW) significance $\sigma \geq 3$ from the STIS and UVES echelle spectra across both lines-of-sight.

All of the Ly- α absorbers below $z = 1.51$ were found in the STIS data and are the 135 lines that were used in the cross-correlation function. Those above are from the UVES spectrum and hence are all from the HE 1122-1648 sightline.

Those below $z = 0.86$ were found in the blue STIS data set that covered the wavelength range $2050 - 2382 \text{ \AA}$ and so are also only from HE 1122-1648. The asterisks mark the redshifts of quasars PKS 1127-145 and HE 1122-1648 at $z = 1.187$ and $z = 2.4$ respectively.

Three factors affect the shape of this histogram. The line-density distribution only evolves slowly out to redshifts $z \sim 1.6$ and then increases rapidly (Janknecht et al. 2006).

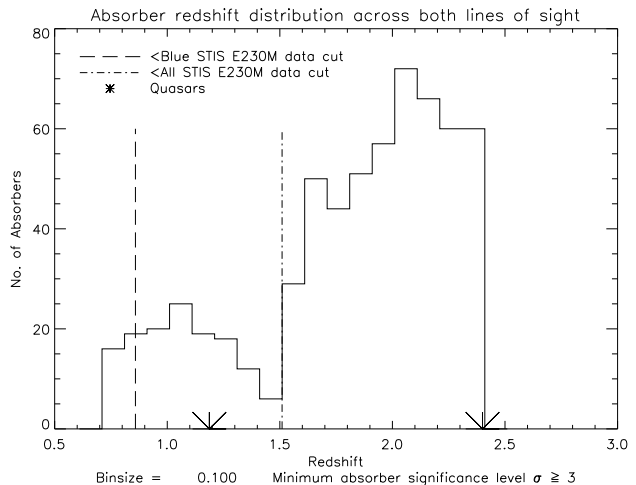


Figure 10. This histogram binned by 0.1 in redshift shows the distribution of all Ly- α absorbers with significance $\sigma \geq 3$ detected across both lines of sight and both the STIS and UVES instruments. The dashed-dot line marks the redshift cut-off between the two instruments and Ly- α absorbers above this were only found along the sightline of HE 1122-1648. Ly- α absorbers below the long dashed line were found in the low wavelength HE 1122-1648 dataset, a damped Lyman system prevented any more absorbers being detected with a redshift below $z = 0.68$. No echelle STIS data below a redshift of $z = 0.896$ existed for QSO PKS 1127-145. The asterisks mark the redshift of quasars PKS 1127-145 at $z = 1.187$ and HE 1122-1648 at $z = 2.4$.

Our data agrees with this result within the error margin. Our data is from only two sightlines, one of which terminates at $z = 1.187$, but also the deficit of lines at $z \sim 1.5$ is attributed to the decreasing S/N and low sensitivity at the extreme red end of the STIS spectra of HE 1122-16478 (see Figure 7).

The increase in the line density above $z = 1.5$ was also due to the increased sensitivity and S/N of the UVES instrument.

5.3 Combining the Ly- α Absorber and Galaxy datasets

Figure 11 shows the location of both galaxies and absorbers across each sight line.

The maximum impact parameter (~ 5000 kpc) shows the distance out to which the correlation function was calculated, and also explains why so few pairs were found in the highest separation bin. Only those galaxies with a redshift $z \gtrsim 1$ could achieve this separation.

Pairs that were used for the correlation function had a maximum line of sight separation of 20 co-moving h_{70}^{-1} Mpc. At a redshift of $z \sim 1$ this equates to $\Delta z \sim 0.05$. Therefore each absorber in the Pie diagrams was only paired with galaxies within a very narrow redshift window, the size of which is too small to resolve in Figure 11.

5.3.1 The Proximity Effect

The line-of-sight proximity effect (Bajtlik et al. 1988) describes the process where ionising radiation from a quasar lowers the neutral fraction of HI, thereby decreasing the line-density of Ly- α absorbers. For lines close to the quasar

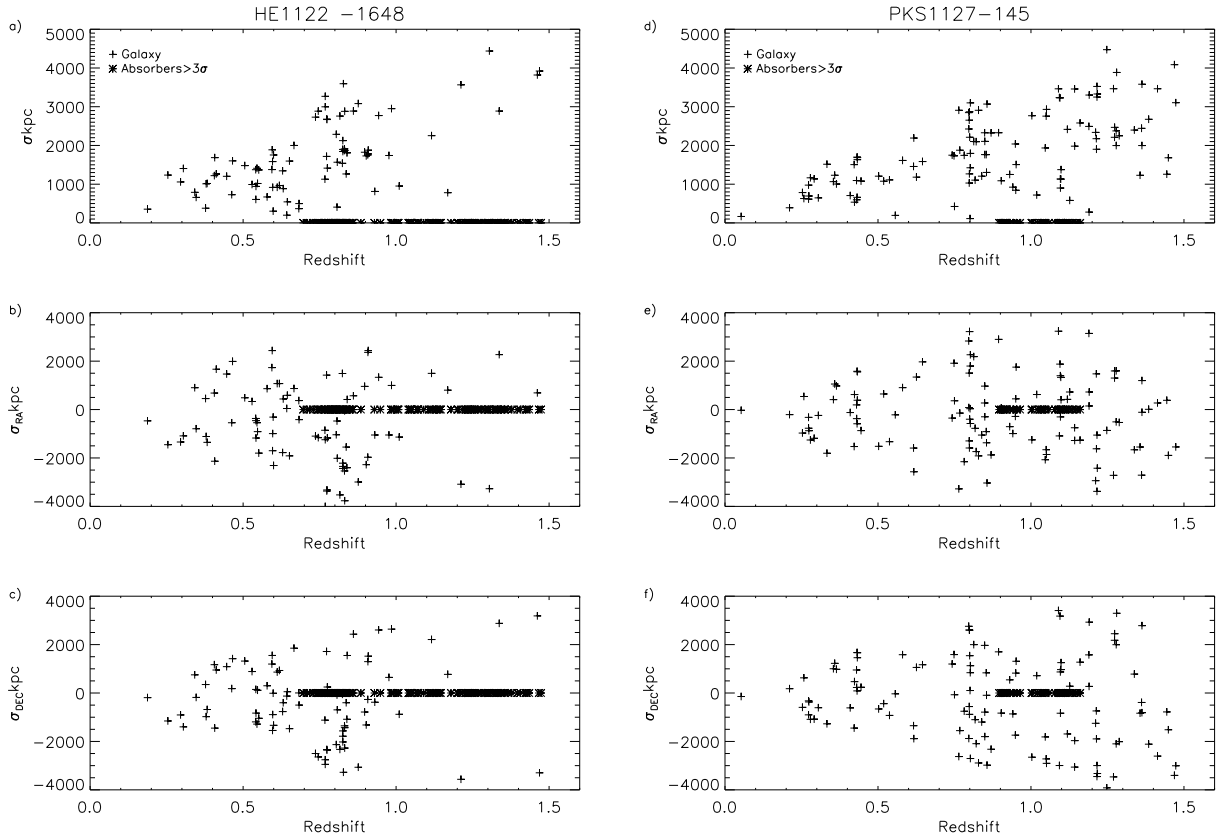


Figure 11. The Pie-diagram for quasar fields HE 1122-1648 and PKS 1127-145. The top panels, plots (a) and (d) show the impact parameter between the galaxy and the quasar sightline plotted as a function of redshift. Panels (b),(e), (c) and (f) show how this separation is split between the RA and DEC of each quasar field respectively. The increasing maximum separation with redshift, observed in plots (a) and (d) mark the boundary of the survey volume. The maximum redshift plotted only covers the overlap between the two populations, so only absorbers from the STIS E230M spectra have been included. The narrower Ly- α absorber redshift window of the PKS 1127-145 field is because of the lower redshift of this quasar.

redshift we may also detect gas that is associated with the quasar itself. This is a concern for the PKS 1127-145 field since galaxies are located near to the QSO redshift. For this reason the 3 Ly- α absorbers and 3 galaxies that were within 3000 km s^{-1} (Chen & Mulchaey 2009) of the quasar were excluded from the line-list and galaxy catalogue when correlating pairs.

5.4 Results for the 2D 2-point Correlation Function

Figure 12(a) shows the 145 real Ly- α absorber-galaxy pairs out to $20 \times 5 \text{ h}_{70}^{-1} \text{ Mpc}$ binned with $\Delta\pi = 2.0$, $\Delta\sigma = 1.0 \text{ h}_{70}^{-1} \text{ Mpc}$. These pairs were made of Ly- α absorbers that had an equivalent width significance of at least 3 and galaxies of a redshift confidence ≤ 4 according to the flags in Table 3.

Above $\sigma \geq 4 \text{ h}_{70}^{-1} \text{ Mpc}$ there were very few real pairs detected. For this reason this last column should be ignored in subsequent plots as the Poisson noise introduced large fluctuations in the results for ξ_{AG} in these bins. Where this occurred the highest value in the colour bar of all of the plots ignores these maxima. Figure 12(b) shows the plot of the normalised RR counts. The DD/RR-1 correlation plot is in Figure 12(c) and the associated error in Figure 12(d).

Binned to this level we can conclude the following.

- For low column density absorbers ($\log_{10} (N_{\text{HI}} (\text{cm}^{-2})) \leq 17.4$ of which only 11 have $\log_{10} (N_{\text{HI}} (\text{cm}^{-2})) \geq 15$), there is no evidence for correlation between the Ly- α absorbers and galaxies. The maximum value in Figure 12(c) was $\xi_{AG} = 2.2 \pm 0.9$ at $\pi = 4 - 6$, $\sigma = 0 - 1 \text{ h}_{70}^{-1} \text{ Mpc}$. So within $20 \times 5 \text{ h}_{70}^{-1} \text{ Mpc}$ a 3σ upper-limit for the cross-correlation is $\xi_{AG} = 2.8$.

The bin with the peak in the correlation function contained 4 real pairs (1.25 random). Excluding the $\sigma = 4 - 5 \text{ h}_{70}^{-1} \text{ Mpc}$ separation 3 bins contained no pairs giving $\xi_{AG} = -1.0$. One of these bins occurred at $\pi = 6 - 8$, $\sigma = 0 - 1 \text{ h}_{70}^{-1} \text{ Mpc}$ with the minimum value of $\xi_{AG} = -1.0 \pm 0.8$. So there is a 2.6σ variation in ξ_{AG} between the maximum and minimum values along the line of sight at $\sigma = 0 - 1 \text{ h}_{70}^{-1} \text{ Mpc}$. A similar variation in ξ_{AG} is also shown at $\sigma = 1 - 2 \text{ h}_{70}^{-1} \text{ Mpc}$ across the same range in values. The values of ξ_{AG} varied from $\xi_{AG} = -0.4 \pm 0.5$ to $\xi_{AG} = 1.9 \pm 0.6$. Comparable values of ξ_{AG} are also found at $\sigma = 2 - 3 \text{ h}_{70}^{-1} \text{ Mpc}$, with a peak of $\xi_{AG} = 0.7 \pm 0.5$. So there are no significant trends observed in the degree of correlation along either axis.

- Binned to this level and at these redshifts obviously we see no evidence for a “finger-of-god” at small projected separation along the line-of-sight.

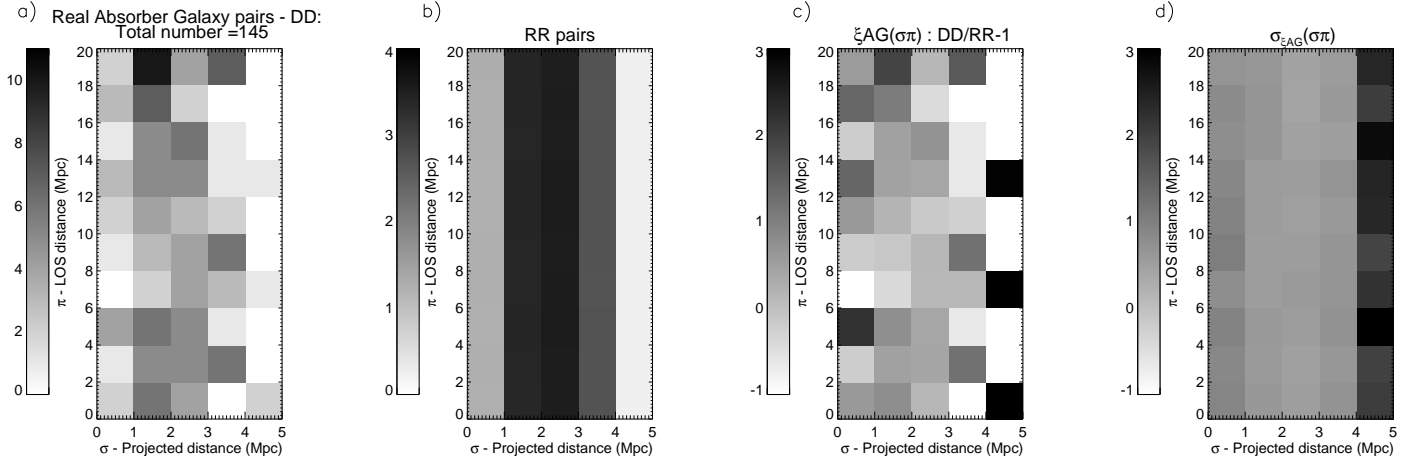


Figure 12. Plot (a) shows the real absorber-galaxy pairs out to $20 \times 5 h_{70}^{-1}$ Mpc, binned $\delta\pi = 2.0 \delta\sigma = 1.0 h_{70}^{-1}$ Mpc. Those galaxies with a maximum confidence level of 4 have been included in this plot, with all Ly- α absorbers with an equivalent width significance $\sigma_{EW} \geq 3$. The 2D 2-point correlation function $\xi_{AG} = DD/RR - 1$ was calculated using 145 pairs. Plot (b) is of the random pairs normalised to the same number of pairs as the real pair data. Plots (c) and (d) show ξ_{AG} and the associated error. There is no evidence for correlation between galaxies and Ly- α absorbers within these distances at this level of binning. A 3σ upper-limit of $\xi_{AG} = 2.8$ was computed using the bin with the maximum value at $\pi = 4 - 6, \sigma = 0 - 1 h_{70}^{-1}$ Mpc. The central bin has a value of $\xi_{AG} = 0.6 \pm 0.9$.

- A result that was shared with Figure 2 of W07 is the suggestion of an off-origin maximum in the correlation for low density absorbers ($\log_{10}(N_{HI}(\text{cm}^{-2})) = 13 - 15$), although this result was also consistent with a correlation equal to 0. The correlation function at the bin of closest separation in Figure 12(c) is $\xi = 0.6 \pm 0.9$. This is only 1.2σ lower than the peak along $\sigma = 0 - 1 h_{70}^{-1}$ Mpc. That both investigations hint at a drop in correlation at small separation is only tentative evidence that low-column density Ly- α absorbers are not observed at short distances. As their column density is so low these absorbers could be easily photo-ionised and stripped of their neutral gas when they enter the halo.

We expect lines of a higher column density to show a greater clustering. However, with such a small line-list and so few absorbers that had $\log_{10}(N_{HI}(\text{cm}^{-2})) \geq 15$ we have not measured the cross-correlation of a sub-set with absorbers that have a higher column density. Only 18 pairs fit this criteria with 2 real pairs in the bin of smallest separation.

5.5 Comparison with the Galaxy Auto-Correlation Function

To compare with the cross-correlation, the galaxy auto-correlation was calculated for all the galaxies with a redshift confidence ≤ 4 that were above a redshift of $z = 0.68$. All literature results point to the galaxy auto-correlation peaking at the smallest separation then decaying in a distorted radial pattern (Pollo et al. 2005; Hawkins et al. 2003; Coil et al. 2006; Guzzo et al. 2008; Zheng et al. 2007).

In the galaxy auto-correlation function the distribution of the random pairs was made by perturbing each real galaxy redshift by a random amount that varied between $\delta z = \pm 0.01 - 0.1$. These boundaries were chosen so that the large-scale redshift distribution was maintained but any

galaxy pair that had existed would now no longer appear within the $20 \times 5 h_{70}^{-1}$ Mpc window.

The plots in Figure 13 show the result of this approach. Plot (a) of Figure 13 are the 138 DD galaxy pairs. Figure 13 plot (b) is of the RR pairs. Plots (c) and (d) show ξ_{GG} and the error, with a central peak of $\xi_{GG} = 10.7 \pm 1.4$.

The value in the central bin of ξ_{GG} is in agreement with other galaxy auto-correlation measurements taken at the same epoch, despite the smaller number of pairs in our sample. For example from the VVDS-Wide survey (Pollo et al. 2005) which contained ~ 6000 galaxy redshifts at $0.6 \leq z \leq 1.2$. The correlation function contained a peak of $\xi_{GG} \gtrsim 10$ in the central bin and a prominent “finger-of-god” along the line of sight (Guzzo et al. 2008).

It is interesting to study the evolution of the galaxy auto-correlation in order to compare this with changes in the Ly- α absorber-galaxy cross-correlation. The auto-correlation at small separation and at redshifts $z \sim 1$ is lower than at more recent epochs because of the gravitational collapse of the halo systems (Zheng et al. 2007). For example Figure 14 shows the auto-correlation of ~ 220000 galaxies at redshifts $0.01 \leq z \leq 0.2$ from the 2dFGRS data (Hawkins et al. 2003). These have been re-binned to match our plots so that the values for ξ_{GG} can be compared.⁶ At redshifts $z \leq 0.2$ the value in the central bin is $\xi_{GG} = 17.4 \pm 2.9$ and there is a significant “finger-of-god” along the line of sight.

An alternative way to convey the difference between the results from Hawkins et al. (2003) and our galaxy survey is to plot the redshift-space correlation parameter $\xi_{GG}(s)$,

⁶ Data supplied by Dr. P. Norberg, Institute for Astronomy, University of Edinburgh.

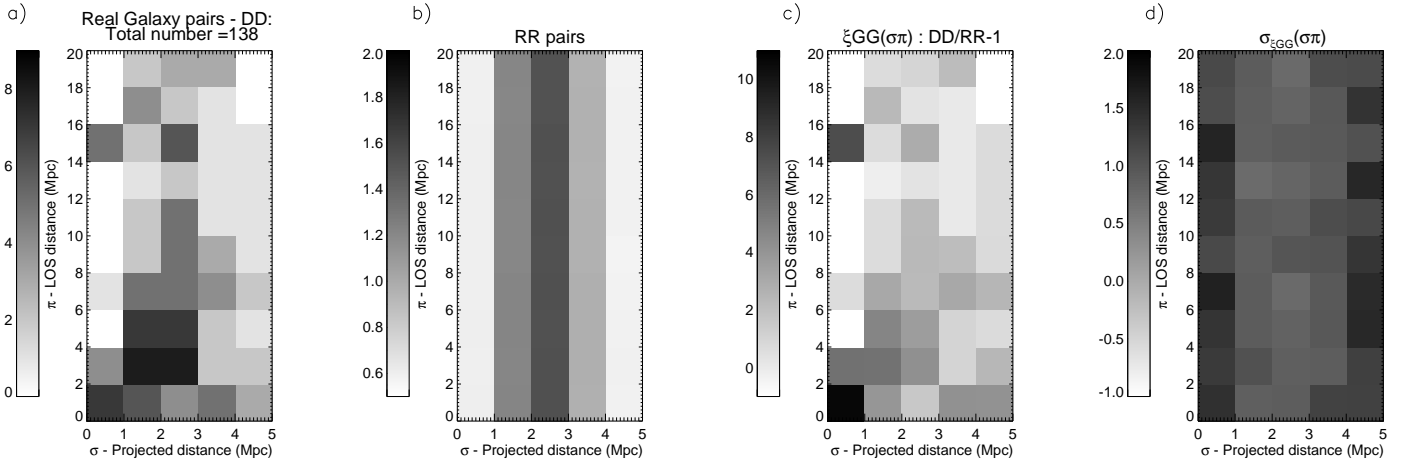


Figure 13. Plots (a) and (b) show the DD and normalised RR pairs that were used for the galaxy auto-correlation function. The redshifts for the RR pairs were created by perturbing each real redshift by $\delta z = \pm 0.01 - 0.1$. Plots (c) and (d) show $\xi_{GG}(\sigma, \pi)$ and the associated error. The peak in the auto-correlation in the bin of smallest separation is $\xi_{GG} = 10.7 \pm 1.4$.

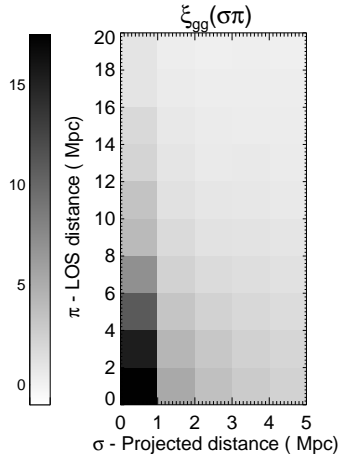


Figure 14. The 2D 2-point auto-correlation ξ_{GG} of the 2dFGRS from Hawkins et al. (2003). The distances have been set to $h=0.7$ and the data re-binned to $\delta\pi = 2.0$, $\delta\sigma = 1.0 h_{70}^{-1}$ Mpc. When compared to figure 13 the values for ξ_{GG} are 2.1σ higher at the centre with a value of $\xi_{GG} = 17.4 \pm 2.9$. We also see a significant “finger-of-god” redshift distortion along $\sigma = 0 - 1 h_{70}^{-1}$ Mpc. An increase in ξ_{GG} is expected at lower redshifts due to gravitational collapse.

where,

$$s = \sqrt{(\pi^2 + \sigma^2)}$$

This is shown in Figure 15.

5.5.1 Comparing the cross and auto-correlation function

When ξ_{AG} from Figure 12(c) is compared with ξ_{GG} from Figure 13(c) we can draw the following conclusion. The values of the central bin have a 5.9σ difference in the level of

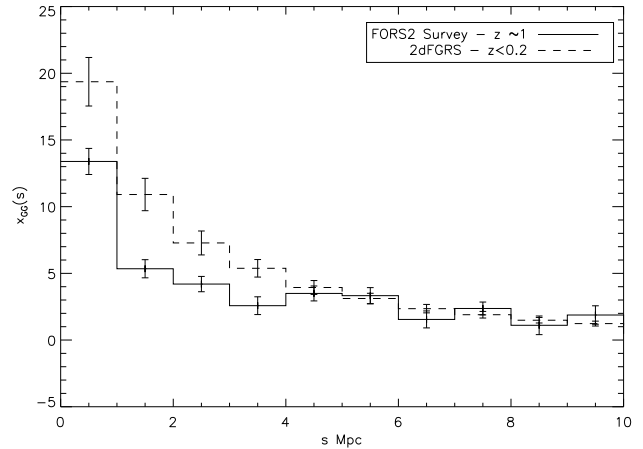


Figure 15. This comparison between the auto-correlation from Hawkins et al. (2003) and our result shows the 1.6σ increase in the auto-correlation $\xi_{GG}(s)$ of the central bin as the redshift has decreased from $z \sim 1$ to ≤ 0.2 .

correlation, with a 5.4σ difference between the central peak of ξ_{GG} and the 3σ upper-limit of ξ_{AG} .

Therefore there is significant evidence of a difference in the cross-correlation between galaxies and Ly- α absorbers and the galaxy auto-correlation on scales of 1 Mpc at redshifts ~ 1 .

To check that our results are not dependent on galaxies with less certain redshifts, the cross and auto-correlation function were recalculated if pairs containing galaxies that had a redshift confidence of 4 were excluded. Galaxies that were identified only using [O II] emission constituted the majority of the 95 galaxies of those that had a redshift greater than $z = 0.68$. This meant that there were too few pairs for both the cross and auto-correlation in each bin. In order to use the much smaller data sample we needed to increase the bin size.

5.6 Variation in the binning and the 1D correlation function along π and σ

5.6.1 Binned $2 \times 2 \text{ h}_{70}^{-1} \text{ Mpc}$

To reduce the effects of shot noise for the smaller galaxy sample we increased the size of each bin. The bin size was increased to $\Delta\pi = \Delta\sigma = 2 \text{ h}_{70}^{-1} \text{ Mpc}$. However, the error in the cross-correlation was still comparable with the data in most bins. These new plots only extend to an impact parameter of $4 \text{ h}_{70}^{-1} \text{ Mpc}$.

Figures 16 and 17 show ξ_{AG} and ξ_{GG} respectively for those galaxies that had a redshift confidence ≤ 3 .

Figure 16 supports the conclusion made earlier. The maximum value in the cross-correlation, not at the central bin, was now at $\pi = 12 - 14$, $\sigma = 0 - 2 \text{ h}_{70}^{-1} \text{ Mpc}$ with a value of 0.7 ± 0.6 . Therefore when binned to this extent there was only a weak correlation between Ly- α absorbers and galaxies. We found a 3σ upper-limit of $\xi_{AG} = 1.9$.

Comparisons with the galaxy auto-correlation also remained the same. When binned to $\Delta\pi = \Delta\sigma = 2 \text{ h}_{70}^{-1} \text{ Mpc}$, (where averaging over $2 \text{ h}_{70}^{-1} \text{ Mpc}$ along σ caused ξ_{GG} to decrease), in the central bin there is still stronger clustering amongst galaxies than between galaxies and Ly- α absorbers at a 6.0σ level of confidence. The central bin in the auto-correlation now had a value of $\xi_{GG} = 7.4 \pm 1.0$.

When the galaxies with a redshift confidence ≤ 4 were used at this level of binning no significant difference was observed. The cross and auto-correlation had values in the central bin of $\xi_{AG} = 0.7 \pm 0.5$ and $\xi_{GG} = 6.1 \pm 0.7$ respectively.

5.6.2 Summed over the line of sight and projected separation

In order to further reduce the Poisson error in the correlation function we collapsed the pair counts along each dimension entirely. As in the previous section, in order to maximise the number of pairs, we include galaxies with a redshift confidence ≤ 4 .

Plots (a), (b) and (c) of Figure 18 show the number of real pairs, the number of random pairs and ξ_{AG} when binned along the projected separation with $\Delta\sigma = 0.5 \text{ h}_{70}^{-1} \text{ Mpc}$. This is the projected correlation $\Xi(\sigma)$ where;

$$\Xi(\sigma) = \int_0^{\infty} \xi(\sigma, \pi) d\pi$$

In practice the upper limit was taken to be the maximum separation of the pairs when binned in the 2D plots, $\pi = 20 \text{ h}_{70}^{-1} \text{ Mpc}$. The absolute separation between the absorbers and galaxies was used, therefore the lower limit was zero.

By summing over the line of sight we also removed any peculiar velocity distortions that may have been present since these only displace pairs along the π axis.

The general shape of plot (a) of Figure 18 supports what has already been mentioned in Section 5.1. As the survey volume increased the number of galaxies, hence the number of pairs also increased. This peaked between $1-2 \text{ h}_{70}^{-1} \text{ Mpc}$ before decreasing because galaxies were now located at the edge of the surveyed region. The smaller number of pairs at $\sigma = 2 - 2.5 \text{ h}_{70}^{-1} \text{ Mpc}$ is real and can be deduced from the

Pie-diagrams in Figure 11. In the field of view of HE 1122-1648 there were only 4 galaxies that were at a separation of $2 - 2.5 \text{ h}_{70}^{-1} \text{ Mpc}$. In the field of PKS 1127-145 there were 20, however only 4 of these were between the same redshift range as the absorbers.

The offset peak in plot (c) of Figure 18 at $\sigma = 1 \rightarrow 1.5 \text{ h}_{70}^{-1} \text{ Mpc}$ could be tentative evidence that low column density absorbers are more scarce the closer the distance to a galactic halo. However this peak is not significant with an increase of only 1.3σ from $\sigma = 0 - 0.5 \text{ h}_{70}^{-1} \text{ Mpc}$. The level of correlation then remained the same, as there was no significant change in $\Xi_{AG}(\sigma)$ out to $\sigma = 4 \text{ h}_{70}^{-1} \text{ Mpc}$. The 2 bins above $\sigma = 4 \text{ h}_{70}^{-1} \text{ Mpc}$ have been ignored in this comparison as only 4 real pairs were found beyond this distance.

When binned using $\Delta\pi = 2 \text{ h}_{70}^{-1} \text{ Mpc}$ along the line of sight, the weak correlation $\xi_{AG}(\pi)$ shown in plot (f) of Figure 18 did not have any significant change in value as π increased from $0 - 20 \text{ h}_{70}^{-1} \text{ Mpc}$.

6 DISCUSSION AND CONCLUSION

The two straw-man models mentioned in the introduction were that the gas follows the galaxy distribution and collects in galaxy haloes, or it forms part of a diffuse network, located near but not necessarily causally linked with galaxies.

Figure 12 showed that we did not detect significant correlation between galaxies and Ly- α absorbers that have $13 \leq \log_{10}(\text{N}_{\text{HI}}(\text{cm}^{-2})) \leq 17.4$. As only 145 absorber-galaxy pairs existed within $\Delta\sigma = 0 - 5$, $\Delta\pi = 0 - 20 \text{ h}_{70}^{-1} \text{ Mpc}$, in Figure 12(a), no cuts in the column density were made as this would further increase an already large uncertainty. An overwhelming majority of the Ly- α absorbers from the STIS spectra however had $\log_{10}(\text{N}_{\text{HI}}(\text{cm}^{-2})) \leq 15$.

We calculated a 3σ upper-limit of $\xi_{AG} = 2.8$. The decrease in the 3σ upperlimit to 1.9 in Figure 16, caused by the increase in binsize to $\Delta\sigma = \Delta\pi = 2 \text{ h}_{70}^{-1} \text{ Mpc}$ is further evidence that ξ_{AG} is near to 0 when averaged over these distances. This result was supported by the 1D plots of $\xi_{AG}(\pi)$ and $\Xi_{AG}(\sigma)$ along the line of sight and projected separation in Figure 18.

The value in the central bin for the galaxy auto-correlation function was $\xi_{GG} = 10.7 \pm 1.4$. This was a 5.9σ increase on the value in the equivalent bin of the absorber-galaxy cross-correlation that had a value of $\xi_{AG} = 0.6 \pm 0.9$.

Even when the value for the auto-correlation was reduced by the larger binning in Figure 17, the difference between the 3σ upper-limit in the cross correlation and the central bin in the auto-correlation was still 5.5σ .

This evidence implies that at a redshift of $z \sim 1$ galaxies that inhabit the nodes and filaments of the dark matter cosmic web are not strongly correlated with the low column density Ly- α absorbers ($\log_{10}(\text{N}_{\text{HI}}(\text{cm}^{-2})) \leq 17$) that loosely trace this filamentary structure.

With a catalogue of 95 galaxies within a redshift range of $z = 0.68 - 1.51$ that produced 138 galaxy pairs, it is unlikely that we would have been able to reproduce the result and distribution of pairs of the galaxy auto-correlation function found by Pollo et al. (2005) and Guzzo et al. (2008). However our results were similar within the margin of error. When these studies are compared with the results at $z \leq 0.2$ there is a noticeable decrease in the auto-correlation.

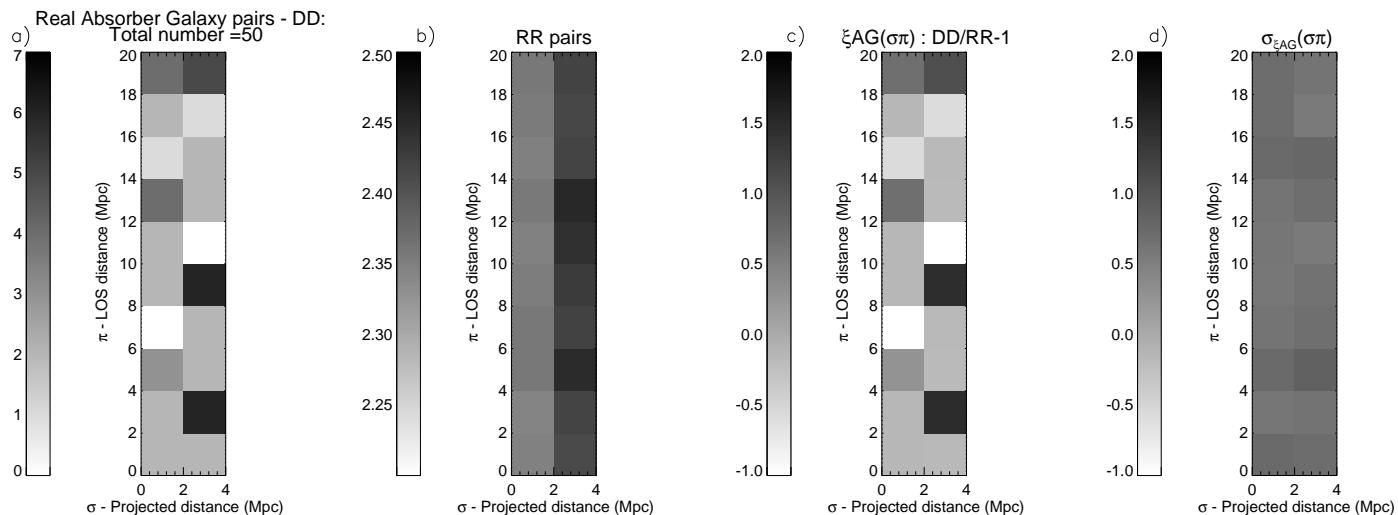


Figure 16. Plots a-d are of the 50 absorber-galaxy DD pairs, RR pairs, $\xi_{AG}(\sigma, \pi)$ and error respectively when the level of binning has been increased to $\Delta\pi = \Delta\sigma = 2 h_{70}^{-1}$ Mpc. The error per bin has decreased and the peak in correlation is now 0.7 ± 0.6 at $\pi = 12 - 14$, $\sigma = 0 - 2 h_{70}^{-1}$ Mpc. The result is the same as to what was observed in Figure 12. This negligible degree of correlation also does not change significantly along the line of sight as the value varies by $\sim 1\sigma$ only. Values for ξ_{AG} also do not significantly change when at a projected separation of $\sigma = 2 - 4 h_{70}^{-1}$ Mpc.

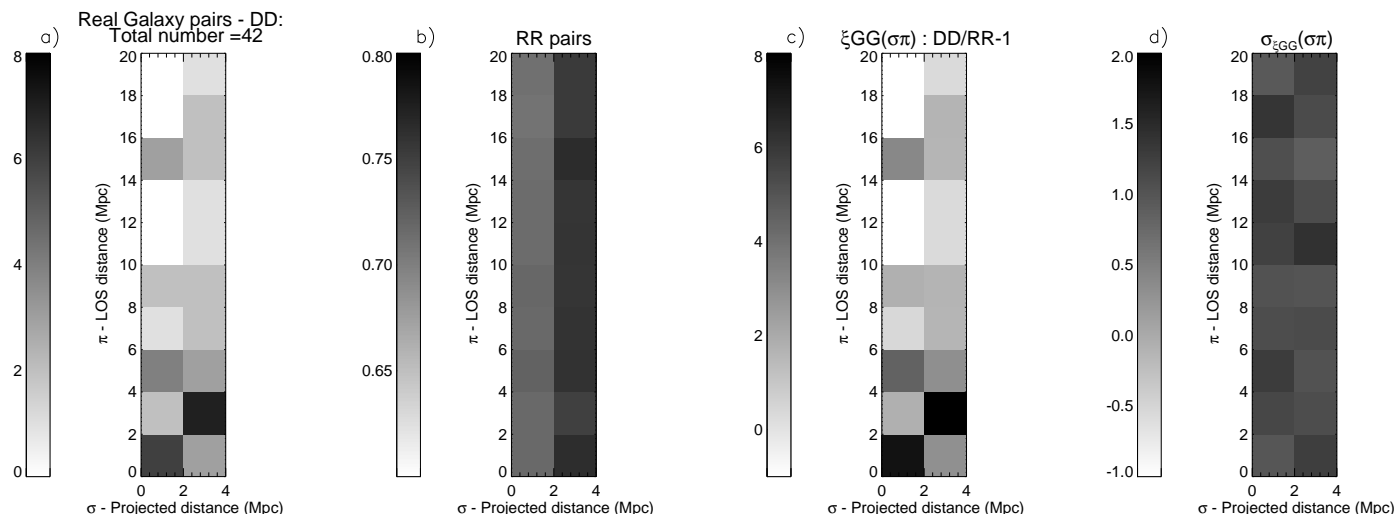


Figure 17. Plots a-d are of the 42 real galaxy pairs, DD, random-random galaxy pairs, RR, and the galaxy auto-correlation, ξ_{GG} and error respectively. When binned $\Delta\pi = \Delta\sigma = 2 h_{70}^{-1}$ Mpc the same conclusions can be drawn for the auto-correlation function. Correlation between galaxies decreased along the line of sight, until after $\pi \sim 6 h_{70}^{-1}$ Mpc the correlation signal was comparable with $\xi_{AG}(\sigma, \pi)$.

When our results are compared with the values of the cross-correlation at redshifts $\lesssim 0.5$ the data suggest that the cross-correlation between low column density Ly- α absorbers and galaxies does not have a strong redshift dependence. This may be because of the flat evolution in the Ly- α absorber density distribution at redshifts $\lesssim 1.7$ (Janknecht et al. 2006).

This conclusion is a stark contrast to that which was found by RW06. In that investigation ξ_{AG} had been found to be comparable with ξ_{GG} with values ≈ 11 in the closest bin. There are three possible reasons for this difference. First of all the dataset of RW06 was at low redshift, where clustering is thought to have increased because of gravitational col-

lapse. However an increase of this magnitude over a change in redshift of $z \sim 1 \rightarrow 0$ does not seem plausible, particularly when results gathered by Wilman et al. (2007), Chen et al. (2005); Chen & Mulchaey (2009) and Pierleoni et al. (2008) cite lower values for ξ_{AG} at redshifts of $z \lesssim 0.5$ and 0.

Another reason may be because of the galaxy population. RW06 used the HIPASS galaxies that were detected using 21 cm emission and targeted in a blind survey. Therefore as well as being gas rich it included galaxies of any mass. Hence a strong correlation and velocity dispersion along the line-of-sight were expected as gas falls through the potential of the filamentary structure and is accreted directly by

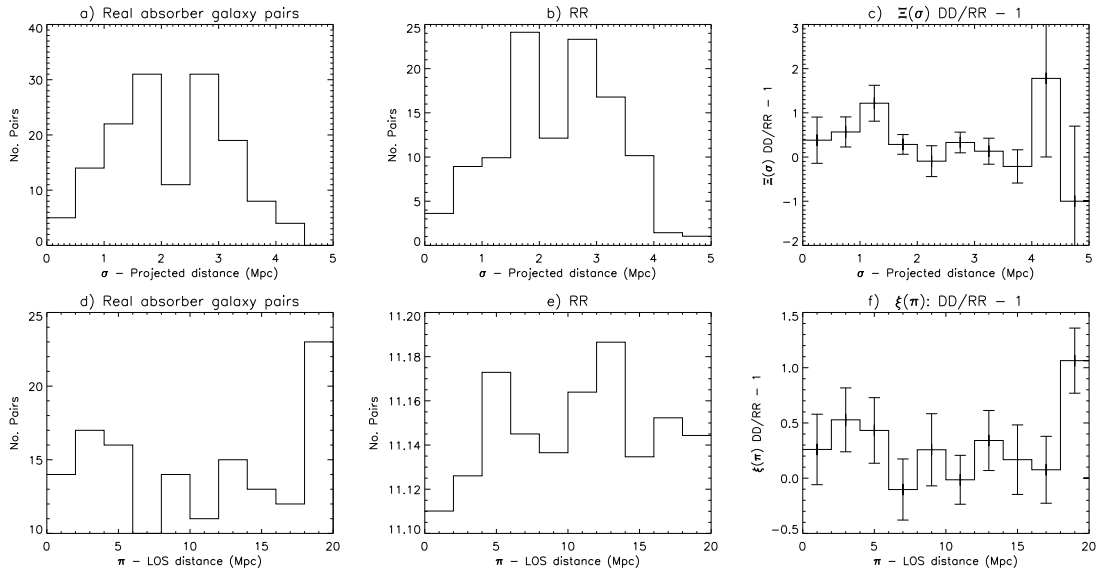


Figure 18. Plots (a) and (b) show the number of DD and RR absorber-galaxy pairs when they are binned along the projected separation. The shape of these histograms are a consequence of the edge effects discussed and illustrated in figure 9. The lack of pairs at $\sigma = 2.5 h_{70}^{-1}$ Mpc is compensated in plot (b) by using the perturbed redshift technique. Plot (c) suggests an off-centre peak in the cross-correlation at $\sigma = 1 - 1.5 h_{70}^{-1}$ Mpc. This peak is not significant with an increase of only 1.3σ from $\sigma = 0 - 0.5 h_{70}^{-1}$ Mpc. There is no significant change in $\Xi_{AG}(\sigma)$ out to $\sigma = 4 h_{70}^{-1}$ Mpc. Plots (d) and (e) show the number of DD and RR absorber-galaxy pairs when binned along the line of sight. Plot (f) shows the cross-correlation, $\xi_{AG}(\pi)$ in steps of $\delta\pi = 2 h_{70}^{-1}$ Mpc. At these levels of significance there is no evidence for any correlation between the galaxies and low column density absorbers. What is important is this lack of correlation is constant along the line of sight with a variance of less than 1σ as π increases from $0-18 h_{70}^{-1}$ Mpc.

the low-mass galaxies. This is the method of ‘cold-accretion’ proposed in Kereš et al. (2005).

Our magnitude limited galaxies ($M_B \sim -17 \rightarrow -21$) were collected in an incomplete survey at higher redshifts than that of the HIPASS catalogue. Consequently the galaxies for which we were able to get spectroscopic data would have a higher mass than most of the HIPASS candidates. Kereš et al. (2005) claim that the dominant mode of accretion for galaxies with a dark halo mass $M \gtrsim 10^{11.4} M_{\odot}$ is the more conventional method; where gas is shock heated to the virial temperature of the halo before cooling and collapsing onto the galaxy. This could mean less neutral gas is expected in the immediate vicinity of the galaxies in our sample when compared to those from RW06.

Another reason why the cross-correlation may seem larger in Ryan-Weber (2006) is because of the smaller bin size of $\Delta\sigma = \Delta\pi = 0.1 h_{100}^{-1}$ Mpc that was used. We could argue that the absorbers that are at $\sigma < 0.1 h_{100}^{-1}$ Mpc are contained within the galaxy halo and may even be virialised, so ξ_{AG} per bin is likely to substantially increase.

Alternatively these discrepancies could be due to the problem suggested by Pierleoni et al. (2008). Ryan-Weber (2006); Wilman et al. (2007); Chen et al. (2005); Chen & Mulchaey (2009) and to a greater extent our dataset all either contain few pairs and/or few lines-of-sight. The appearance or absence of artifacts such as a strong ‘finger-of-god’ in the correlation pattern could be due to the small size of the sample.

Unfortunately because we only had 13 galaxies in the catalogue that were dominated by absorption features we were unable to test the hypothesis of Chen et al. (2005) and Chen & Mulchaey (2009) that ξ_{AG} is stronger for those

galaxies that are dominated by emission and comparable to the emission dominated galaxy auto-correlation function. However we still see a low correlation in the smallest bin, despite the abundance of emission dominated galaxies in our sample.

We are hoping to improve on these findings with more data collected from three further STIS E230M lines-of-sight and galaxies from the VIMOS instrument. This will enable us to correlate galaxies and Ly- α absorbers out to a projected separation of $\sigma \sim 7 h_{70}^{-1}$ Mpc at a redshift of $z \sim 1$. We also plan to investigate the 2D 2-point correlation function using the Galaxies-Intergalactic Medium Interaction Calculation (GIMIC) SPH simulation (Crain et al. 2009).

7 A SUMMARY OF THE RESULTS ON THE 2 POINT CORRELATION FUNCTION

We have set the first limits on the 2D 2-point correlation function between Ly- α absorbers of a column density $13.2 \leq \log_{10}(N_{\text{HI}} \text{ cm}^{-2}) \leq 17.4$ and galaxies from a magnitude limited survey of $21.5 \leq R \leq 24.5$ at $z \sim 1$, and have compared this result to the galaxy auto-correlation.

When binned over both the projected separation and line of sight out to 5 and $20 h_{70}^{-1}$ Mpc respectively with $\Delta\sigma = 1$, $\Delta\pi = 2 h_{70}^{-1}$ Mpc, there was no sign at a 3σ level for any significant correlation. The peak value at $\sigma = 0-1$, $\pi = 4-6 h_{70}^{-1}$ Mpc gave a 3σ upper-limit of $\xi_{AG}(\sigma\pi) = 2.8$. A 5.4σ difference was found between this upper-limit and our value for the galaxy auto-correlation function. This result is robust even when we remove subsets of the galaxy sample that have less secure redshifts.

Our value for the galaxy auto-correlation, $\xi_{GG} = 10.7 \pm 1.4$ at $\sigma = 0 - 1$, $\pi = 0 - 2 \text{ h}_{70}^{-1} \text{ Mpc}$ was consistent with the VVDS-Wide Survey that was taken at the same epoch. Both of these surveys show a lower level of correlation than that of the 2dFGRS survey at redshifts $z \leq 0.2$, which is consistent with the evolution that is expected.

We found no difference between our results and ξ_{AG} found by Wilman et al. (2007) who studied ξ_{AG} at $z \sim 0.5$. Thus our results are consistent with there being no significant evolution in ξ_{AG} with redshift. The much greater value of ξ_{AG} found by Ryan-Weber (2006) at $z = 0$ that was comparable to ξ_{GG} could be because the galaxies in her sample were gas rich and have a lower mass.

ACKNOWLEDGEMENTS

Our thanks go to Robert Carswell for his support and suggestions when using VPFIT.

Some of the data presented in this paper were obtained from the Multimission Archive at the Space Telescope Science Institute (MAST). STScI is operated by the Association of Universities for Research in Astronomy, Inc., under NASA contract NAS5-26555. Support for MAST for non-HST data is provided by the NASA Office of Space Science via grant NAG5-7584 and by other grants and contracts.

The work in this paper was supported in part by an STFC PhD studentship.

REFERENCES

- Adelberger K. L., Shapley A. E., Steidel C. C., Pettini M., Erb D. K., Reddy N. A., 2005, **ApJ**, 629, 636
- Adelberger K. L., Steidel C. C., Shapley A. E., Pettini M., 2003, **ApJ**, 584, 45
- Appenzeller I., Fricke K., Fürtig W., Gässler W., Häfner R., Harke R., Hess H.-J., Hummel, W. et al., 1998, *The Messenger*, 94, 1
- Bahcall J. N., Jannuzi B. T., Schneider D. P., Hartig G. F., Bohlin R., Junkkarinen V., 1991, **ApJL**, 377, L5+
- Bajtlik S., Duncan R. C., Ostriker J. P., 1988, **ApJ**, 327, 570
- Bechtold J., Dobrzycki A., Wilden B., Morita M., Scott J., Dobrzycka D., Tran K.-V., Aldcroft T. L., 2002, **ApJS**, 140, 143
- Bertin E., Arnouts S., 1996, **A&AS**, 117, 393
- Bregman J. N., 2007, **Annu. Rev. Astron. Astrophys.**, 45, 221
- Bruzual G., Charlot S., 2003, **MNRAS**, 344, 1000
- Carswell B., Schaye J., Kim T.-S., 2002, **ApJ**, 578, 43
- Cen R., Ostriker J. P., 1999, **ApJ**, 514, 1
- Chen H., Lanzetta K. M., 2003, **ApJ**, 597, 706
- Chen H., Mulchaey J. S., 2009, **ApJ**, 701, 1219
- Chen H., Prochaska J. X., Weiner B. J., Mulchaey J. S., Williger G. M., 2005, **ApJL**, 629, L25
- Cohen J. G., Hogg D. W., Blandford R., Cowie L. L., Hu E., Songaila A., Shopbell P., Richberg K., 2000, **ApJ**, 538, 29
- Coil A. L., Gerke B. F., Newman J. A., Ma C.-P., Yan R., Cooper M. C., Davis M., Faber, S. M. et al., 2006, **ApJ**, 638, 668
- Crain R. A., Theuns T., Dalla Vecchia C., Eke V. R., Frenk C. S., Jenkins A., Kay S. T., Peacock, J. A. et al., 2009, **MNRAS**, 399, 1773
- Cristóbal-Hornillos D., Balcells M., Prieto M., Guzmán R., Gallego J., Cardiel N., Serrano Á., Pelló R., 2003, **ApJ**, 595, 71
- Dall’Aglio A., Wisotzki L., Worseck G., 2008, **A&A**, 491, 465
- Danforth C. W., Shull J. M., 2005, **ApJ**, 624, 555
- Danforth C. W., Shull J. M., 2008, **ApJ**, 679, 194
- Davis M., Peebles P. J. E., 1983, **ApJ**, 267, 465
- Deharveng J.-M., Buat V., Bergeron J., 1995, **A&A**, 298, 57
- Fang T., Mckee C. F., Canizares C. R., Wolfire M., 2006, **ApJ**, 644, 174
- Fukugita M., Hogan C. J., Peebles P. J. E., 1998, **ApJ**, 503, 518
- Guzzo L., Pierleoni M., Meneux B., Branchini E., Le Fèvre O., Marinoni C., Garilli B., Blaizot, J. et al., 2008, **Nature**, 451, 541
- Hawkins E., Maddox S., Cole S., Lahav O., Madgwick D. S., Norberg P., Peacock J. A., Baldry, I. K. et al., 2003, **MNRAS**, 346, 78
- Hogg D. W., Pahre M. A., McCarthy J. K., Cohen J. G., Blandford R., Smail I., Soifer B. T., 1997, **MNRAS**, 288, 404
- Janknecht E., Reimers D., Lopez S., Tytler D., 2006, **A&A**, 458, 427
- Jehin E., O’Brien K., 2007, FORS User Manual, Doc. No. VLT-MAN-ESO-13100-1543. ESO
- Kacprzak G. G., Churchill C. W., Steidel C. C., Murphy M. T., Evans J. L., 2007, **ApJ**, 662, 909
- Kaufer A., D’Odorico S., Kaper L., Ledoux C., James G., 2007, UV-Visual Echelle User Manual, Doc. No. VLT-MAN-ESO-13200-1825. ESO
- Kelson D. D., 2003, **PASP**, 115, 688
- Kereš D., Katz N., Weinberg D. H., Davé R., 2005, **MNRAS**, 363, 2
- Keyes C., Koratkar A., M. D., Hayes J., Christensen J., Martin S., 1995, Faint Object Spectrograph Instrument Handbook. The STScI FOS Group: Baltimore STScI
- Kim T., Carswell R. F., Cristiani S., D’Odorico S., Giallongo E., 2002, **MNRAS**, 335, 555
- Kim Quijano et al. J., 2007, STIS Instrument Handbook, Version 8.0. Baltimore: STScI
- Kirkman D., Tytler D., Lubin D., Charlton J., 2007, **MNRAS**, 376, 1227
- Kurtz M. J., Mink D. J., 1998, **PASP**, 110, 934
- Lanzetta K. M., Bowen D. V., Tytler D., Webb J. K., 1995, **ApJ**, 442, 538
- Le Brun V., Bergeron J., Boisse P., Deharveng J. M., 1997, **A&A**, 321, 733
- Lehner N., Savage B. D., Richter P., Sembach K. R., Tripp T. M., Wakker B. P., 2007, **ApJ**, 658, 680
- Morris S. L., Jannuzi B. T., 2006, **MNRAS**, 367, 1261
- Morris S. L., Weymann R. J., Dressler A., McCarthy P. J., Smith B. A., Terrile R. J., Giovanelli R., Irwin M., 1993, **ApJ**, 419, 524
- Morton D. C., 2003, **ApJS**, 149, 205
- Murphy M. T., Tzanavaris P., Webb J. K., Lovis C., 2007, **MNRAS**, 378, 221
- Nicastro F., Zezas A., Drake J., Elvis M., Fiore F., Frus-

- cione A., Marengo M., Mathur, S. et al., 2002, **ApJ**, 573, 157
- Pettini M., Ellison S. L., Steidel C. C., Bowen D. V., 1999, **ApJ**, 510, 576
- Pettini M., Shapley A. E., Steidel C. C., Cuby J., Dickinson M., Moorwood A. F. M., Adelberger K. L., Giavalisco M., 2001, **ApJ**, 554, 981
- Pierleoni M., Branchini E., Viel M., 2008, **MNRAS**, 388, 282
- Pollo A., Meneux B., Guzzo L., Le Fèvre O., Blaizot J., Cappi A., Iovino A., Marinoni, C. et al., 2005, **A&A**, 439, 887
- Rao S. M., Nestor D. B., Turnshek D. A., Lane W. M., Monier E. M., Bergeron J., 2003, **ApJ**, 595, 94
- Ryan-Weber E. V., 2006, **MNRAS**, 367, 1251
- Sargent W. L. W., Young P. J., Boksenberg A., Tytler D., 1980, **ApJS**, 42, 41
- Schaye J., Carswell R. F., Kim T.-S., 2007, **MNRAS**, 379, 1169
- Schneider D. P., Hartig G. F., Jannuzi B. T., Kirhakos S., Saxe D. H., Weymann R. J., Bahcall J. N., Bergeron, J. et al., 1993, **ApJS**, 87, 45
- Sembach K. R., Tripp T. M., Savage B. D., Richter P., 2004, **ApJS**, 155, 351
- Thom C., Chen H., 2008, **ApJ**, 683, 22
- Tripp T. M., Savage B. D., 2000, **ApJ**, 542, 42
- Verner D. A., Tytler D., Barthel P. D., 1994, **ApJ**, 430, 186
- Wilman R. J., Morris S. L., Jannuzi B. T., Davé R., Shone A. M., 2007, **MNRAS**, 375, 735
- Zheng Z., Coil A. L., Zehavi I., 2007, **ApJ**, 667, 760
- Zwaan M. A., Staveley-Smith L., Koribalski B. S., Henning P. A., Kilborn V. A., Ryder S. D., Barnes D. G., Bhathal, R. et al., 2003, **AJ**, 125, 2842
- Zwaan M. A., van der Hulst J. M., Briggs F. H., Verheijen M. A. W., Ryan-Weber E. V., 2005, **MNRAS**, 364, 1467

This paper has been typeset from a $\text{\TeX}/\text{\LaTeX}$ file prepared by the author.